THESIS

CAVITY RING-DOWN SPECTROSCOPY MEASUREMENTS OF NH_2 IN A PULSED NANOSECOND AMMONIA PLASMA REACTOR

Submitted by

Brian Harrod

Department of Mechanical Engineering

In partial fulfilment of the requirements

for the Degree of Master of Science

Colorado State University

Fort Collins, Colorado

Spring 2026

Master's Committee:

Advisor: Azer Yalin
Co-advisor: Bret Windom

Steve Simske

ABSTRACT

CAVITY RING-DOWN SPECTROSCOPY MEASUREMENTS OF NH_2 IN A PULSED NANOSECOND AMMONIA PLASMA REACTOR

Plasma-reforming of ammonia represents a possible strategy to leverage non-equilibrium plasma kinetics to achieve chemical mixtures that are favorable for combustion applications. Numeric modeling has shown that the amidogen radical (NH_2) is an important radical species in the overall ammonia decomposition kinetics important in both reforming and combustion applications, yet quantitative measurements of the NH_2 radical remain elusive.

The present contribution reports on the development of a compact optically accessible ammonia plasma reactor driven by nanosecond high-voltage pulses. The reactor operated with both pure ammonia and ammonia/nitrogen mixtures (22% NH_3/78% N_2). Experiments were conducted at ammonia flow rates of 3.87 and 45.10 SLPM, with pressures ranging from 71 to 77 Torr. We also report on the development and initial results of NH_2 measurements by the extremely sensitive cavity ring-down spectroscopy (CRDS) laser absorption diagnostic. The cylindrical shaped plasma reactor operates with high voltage pulses (~1.9 to 28 kV) of duration 15 ns delivered at frequencies of ~10-100 kHz. Fast high-voltage probes are used to measure current/voltage traces. The CRDS system is based on a pulsed dye-laser system probing the $^{R}R_{0,2}$ branch of the π vibronic sub-band of the $\tilde{A}^2A_1(0,9,0) \leftarrow \tilde{X}^2B_1(0,0,0)$ transition, and the $^{P}Q_{1,7}$ branch of the □ band of the $\tilde{A}^2A_1(0,9,0) \leftarrow \tilde{X}^2B_1(0,0,0)$ transition. We provide parametric and transient studies of NH_2 densities. Results show the transient nature of NH_2 and the relationship of relative power to NH_2 production. The results will benefit numerical modeling efforts and reactor design focused on

NH_3-plasma systems with applications related to both fuel reforming and plasma-assisted combustion

TABLE OF CONTENTS

CHAPTER 1

INTRODUCTION

1.1 Motivation: Ammonia as a Carbon-Free Energy Source

Green ammonia (NH_3) - produced from green hydrogen and atmospheric or environmental nitrogen, has broad potential to serve as a carbon-free energy source for mobile applications and grid balancing as a renewable energy storage medium. Functioning as a hydrogen fuel carrier, ammonia has a 50% higher energy density than that of pure hydrogen while being 28 times cheaper per kg, primarily due to its ease in transport and storage compared to either liquid or compressed hydrogen [1].

The storage of hydrogen for transportation vehicles has been one of the greatest limitations. The storage of hydrogen as a compressed gas requires a high storage pressure of 240 or 700 bar for stable storage [3]. An alternative storage method is to store hydrogen in the liquid state. However, the output efficiency is greatly reduced, as the process requires 30-40% of the energy present within hydrogen to condense hydrogen to a liquid. In addition, the size of a hydrogen storage vessel must be large in order to maximize its range. The combination of these factors exacerbates safety concerns regarding leak potential or catastrophic failure. Thus, a more efficient means of hydrogen production and storage is required. Functioning as a hydrogen fuel carrier, ammonia has favorable characteristics that distinguish it among alternative chemical fuel storage methods of hydrogen.

The conversion efficiency of a proposed alternative fuel is a critical factor in its viability for specific energy sectors. Hydrogen is a promising alternative fuel, investigated for its abundance and ability to power personal and commercial vehicles. Hydrogen can produce mechanical work in combustion engines and electrical energy from fuel cells [2]. This allows for a wide range of potential applications in the transportation and household utility sectors. However, while the electrochemical conversion of hydrogen in a fuel cell does not produce harmful emissions, 96% of hydrogen production today still relies on fossil fuels, creating greenhouse gases as byproducts [3].

The existing infrastructure currently produces NH_3 in large quantities for use in fertilizers and is produced in a carbon-free process known as the Harber-Bosch process [16]. The Harber-Bosch process works by synthesizing ammonia by combining nitrogen from the atmosphere with hydrogen produced via electrolysis. Ammonia is significantly less expensive to store than liquid or compressed hydrogen as a result of the substantial energy penalty associated with hydrogen compression or liquefaction. Although ammonia appears to be the superior candidate for hydrogen storage, significant complications arise in the combustion phase.

Ammonia's widescale adoption as an energy source, however, has been limited by its tendency to emit high levels of nitric oxides (NO_x - a criteria pollutant) and nitrous oxide (N_2O - a potent greenhouse gas) during end use and its poor combustion characteristics, specifically its resistance to both spark- and autoignition and prohibitively low flame speeds. The combustion efficiencies of ammonia are lower than those of pure hydrogen, which has hindered the adoption of ammonia as a fuel [17]. To allow it to compete with hydrogen as a fuel and justify the lower costs of ammonia, a more efficient combustion strategy for ammonia in ICEs must be implemented. Decomposition of ammonia into radical species through a reformation process directly improves the combustion efficiency of ammonia. Ammonia is a promising carbon-free renewable fuel; however, further validation is required to demonstrate that it is capable of meeting industry standards for energy cost, consumption, and fuel storage requirements when compared to fossil fuels and other renewable fuels.

1.2 Current Applications of Ammonia as a hydrogen carrier

Hydrogen fuel cells have created a promising avenue for efficient energy conversion of hydrogen, generating clean electrical energy for heating, lighting, and cooking [2]. Hydrogen fuel cells can also be used to power transportation, such as the Toyota Mirai [3]. The hydrogen is stored in pressurized tanks, where the energy is then converted to electricity via a hydrogen fuel cell. While hydrogen fuel cells have a higher tank-to-wheel efficiency than hydrogen combustion at low load, cost and efficiency favors hydrogen combustion, meaning a smaller internal combustion engine will outperform a fuel cell of equivalent size when a higher load is applied [4].

Hydrogen as a fuel for ICEs was initially dismissed due to high production costs; however, it has recently emerged as a viable alternative energy carrier [20]. While a fuel cell can be scaled up to be more efficient by operating at low loads, significant complexity and weight is introduced [3]. The benefit of hydrogen in ICE applications is that it can utilize existing infrastructure, and with minimal modifications to the engines. One downside of hydrogen combustion is that combustion requires an oxidizer, typically air, resulting in the production of NO_x emissions, a harmful by-product of typical combustion processes. While carbon emissions are virtually zero, hydrogen combustion still has its downsides.

A combined 65% of greenhouse gas emissions today are directly from the transportation and power generation sectors [2]. Further implementation of hydrogen into these sectors will have a significant impact on harmful emissions globally.

Hydrogen fuel cells and hydrogen combustion both have separate niches in the energy sector. If created in a large enough scale, a hydrogen fuel cell power plant functioning at low loads can have high efficiency, whereas a vehicle combusting hydrogen can utilize existing internal combustion engines or diesel engines operating at higher loads to provide a cheaper and more efficient energy production [3].

Unlike pure hydrogen, ammonia possesses a higher volumetric energy density for fuel storage aboard hydrogen vehicles [5]. Compared with other hydrogen carrier alternatives, ammonia reformation requires a less complex process and produces inert byproducts that can be released into the surroundings. However, it is not without drawbacks. Ammonia is reactive and corrosive in nature, and careful consideration of the materials used to construct an ammonia storage vessel is required [5]. In addition to the storage vessel constraints, PEM fuel cells are extremely sensitive, and the smallest amount of ammonia will significantly affect its performance. A fuel cell also contains components that are susceptible to ammonia corrosion. Consequently, implementing ammonia storage in FCEVs requires a robust mechanism to ensure that no NH_3 reaches the fuel stack [5]. For H2-ICEs, the H2 concentration requirement and complete removal of NH3 is not required [6]. However, stable combustion within ICE's requires 7-11% of the fuel mixture to be hydrogen. This reduces NH_3 emissions but typically results in increased NOx concentrations in the exhaust.

As previously mentioned, hydrogen can be converted to electrical or mechanical energy, making both fuel cells and ICEs viable options for energy generation for the power grid. Two avenues that will be discussed are large scale fuel cells, and hydrogen powered turbine engines.

While current adoption of ammonia as a hydrogen fuel carrier is low, ongoing research into improving ammonia's reformation efficiency is facilitating its integration. As energy conversion of hydrogen in fuel cells and ICEs are constantly improving, they are limited by the inherent storage and cost issues associated with pure hydrogen [6]. Ammonia can greatly reduce the storage issues associated with pure hydrogen, as well as reducing and potentially eliminating the production of harmful NO_X emissions.

Ammonia integration is currently hindered by a limited understanding of the fundamental behavior of ammonia within a reformation process such as plasma reformation. Since ammonia has 45% more hydrogen per volume, if current research leads to an optimized plasma reformation process, ammonia could serve as a dominant sustainable fuel source.

1.3 Fundamentals of Ammonia Combustion Chemistry

Ammonia is characterized by a low laminar burning velocity (0.07 m/s), a high minimum ignition energy (8 mJ), and an elevated auto-ignition temperature of 930 K [7]. These properties of ammonia are key indicators of combustion efficiency and the mechanisms present, and severely inhibit efficient combustion in both spark-ignition and compression-ignition engines due to significant ignition delay for stoichiometric conditions [7], [8]. However, it is still of interest for its hydrogen-carrier properties and makes a promising fuel when cracked pre-combustion. Mixing ammonia with hydrogen has been shown to improve combustion compared to pure ammonia [7]. Co-firing mixtures of ammonia and methane in internal combustion engines or gas turbines can leverage the decarbonization benefits of ammonia while mitigating ammonia's poor combustion efficiency through the addition of methane [7].

Ignition delay is a crucial mechanism of combustion, and careful consideration of ignition delay is required to optimize ammonia for combustion. Significantly decreasing the ignition delay of neat stoichiometric ammonia to levels that risk pre-ignition would require pressures and temperatures beyond the capabilities of modern engines; therefore, uncontrolled premature combustion is not a primary concern for ammonia [7], [8], [9]. The significant ignition delay of neat, stoichiometric ammonia is a key motivation for current and future research on understanding and improving ammonia combustion [8], [9].

In an ammonia study using a common gas burner done by Pugh et al., it was shown that the combustion mechanisms present in of pure ammonia-air mixtures prevent ignition at low temperatures (323 k) without the addition of supplemental hydrogen [8], [10]. Preheating stoichiometric ammonia-air mixtures to 499 K enabled successful ignition in both premixed and non-premixed configurations. Notably, the non-premixed case exhibited increased NH_2 production while simultaneously reducing NOx emissions.

A novel approach to combat the difficulties of combusting pure ammonia is the introduction of a plasma source [8], [11]. Plasma-assisted ammonia combustion in a flame swirler can decrease the required temperature to combust ammonia while increasing the overall flame stability. A direct relationship is also formed between specific energy input of the plasma with NO_x emissions. However, if either voltage or frequency is increased while the other remains constant, NO_x emissions decrease [11].

Past research has applied various reformation techniques to partially convert NH_3 into hydrogen (and accompanying N_2) to promote carbon-free combustion in practical energy conversion devices (e.g., internal combustion engines and gas turbines) [7]. For example, a fuel mixture of 55% NH_3 and 45% H_2 will produce a mixture with a comparable flame speed to that of natural gas. Furthermore, plasma assisted combustion approaches of NH_3 have not only promoted the rate of combustion, but have also reduced NO_x/N_2O emissions to levels seen from typical fossil fuels [11]. In both reforming and oxidation of NH_3, the creation and conversion of the NH_2 radical plays a central role in the chemical kinetics, which has led to numerous studies focused on the development of techniques and approaches to measure NH_2 concentrations within relevant environments [12], [13], [14], [15], [16], [17], [18].

1.4 Ammonia Reformation

1.4.1 Catalytic Reformation

Although direct combustion of ammonia is a possibility, achieving optimal combustion efficiency and minimizing unwanted emissions remains a challenge [19]. Low-temperature ammonia reformation with ruthenium catalysts assisted by cesium has shown promise in generating high hydrogen yields. However, catalyst-based approaches introduce complexity and require precise temperature control, limitations are avoided in plasma reforming [20]. Ideally, ammonia combustion would result solely in nitrogen (N_2) and water (H_2O). Ammonia combustion releases significant concentrations of NO_X gases due to fuel-bound nitrogen and ammonia's complex oxidation kinetics.

1.4.2 Plasma Reformation

Current and ongoing ammonia plasma reformation studies have proven the viability of ammonia as a fuel for ICEs by significantly improving its combustion efficiency when the plasma reformer is used as a pre-combustion aid [11], [21]. Plasma reformation utilizes a nanosecond pulsed plasma across a dielectric cylinder barrier, stimulating electron collisions which dissociate the ammonia into radical species [11], [21], [22]. By controlling ammonia flow and plasma parameters, the efficiency of ammonia reformation can be optimized. HV pulse parameters, specifically Pulse Repetition Frequency (PRF) and Specific Energy input of the pulse (SEI), are crucial for controlling plasma kinetics. Furthermore, a direct relationship exists between the SEI and the amount of NH_3 reformed into hydrogen [21], [23]. The formation of the fuel radical NH_2 in plasma reformation is responsible for producing 90% of the hydrogen in the reformation process and is believed to play a key role in optimizing both the reformation and combustion processes of ammonia.

Optimizing ammonia reforming efficiency can be achieved by manipulating both ammonia flow characteristics and plasma parameters to achieve stable and controllable ammonia decomposition[19], [21]. Plasma discharge properties such as pulse repetition frequency (PRF) and specific energy input (SEI) play a critical role in governing the reforming process[19]. By strategically adjusting these parameters, researchers can potentially maximize the formation of the NH_2 radical. Thereby enhancing overall ammonia conversion efficiency and minimizing unwanted NOx emissions [11], [20].

The Method of ammonia reformation related to this project utilizes a nano-second pulsed plasma to decompose the ammonia into its radical species through electron collisions in a cylindrical dielectric cylinder barrier reactor [11], [22], [23]. The theoretical calculations for the kinetic model are not easily summarized by a formula and are calculated using complex solver programs [22], [23]. Figure 1 provides a concise visual summary of ammonia and oxygen entering a high-energy plasma in which the kinetic reactions produce the reformate species through a catalytic process.

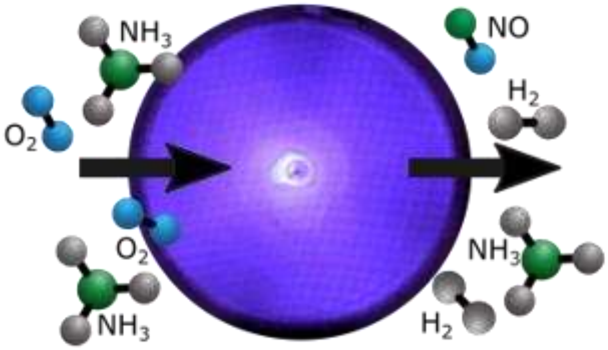

Figure 1: Plasma reformation of ammonia and oxidizer (0_2) [19]

Controlling the ratios of desired reformates, temperature, pressure, and oxidation excess are critical parameters for optimizing plasma reformation [24]. Molecular hydrogen production can be optimized, and NO_x minimized, by determining the oxidant excess coefficient where the mass flowrate of the oxidizer is such that it allows for stable ammonia combustion in air, which is relatively close to a mass flow rate that minimizes NO_X production [24]. The reduction of NO_X emissions can be attributed to increased concentrations of NH_2 [11].

PRF (Pulse Repetition Frequency) is a crucial variable in controlling plasma combustion. The PRF is the rate at which the high-voltage pulse is sent through the chamber, controlling the conditions of the plasma [22]. PRF increases concentrations of NH_2 production in the reformation process which contributes the majority of the reformate hydrogen [19], [23]. As PRF increases, it can increase the decomposition rate of ammonia. NH_2 concentration can be increased by higher pulse repetition frequencies, as well as the addition of an oxidizer, such as air, to the ammonia stream acting as a decomposition catalyst. However a stable PRF will be required, excessively high frequencies may induce thermal runaway, while frequencies that are too low may result in ignition delays [22], [23]. Both contribute to unideal reformation conditions [22]. By controlling the fuel mixture and plasma conditions, the ideal combustion process of ammonia maximizes H_2 in the pre-combustion phase, as well as maximizes the production of ideal combustion by-products in the exhaust, such as H_20 and N_2 while significantly reducing NO_X [22], [25]. By measuring the concentrations of NH_2, we can develop a reformation process that achieves that goal.

The transient nature of NH_2 within the plasma has prohibited the direct measurement of in-situ NH_2 concentration measurements of the NH_2 radical in existing plasma reformers. This investigation leverages cavity ring-down spectroscopy (CRDS), a highly sensitive, non-intrusive, multi-pass laser absorption technique, to quantify NH_2 radical concentrations within the ammonia plasma reformer. The suitability of CRDS for this application stems from its ability to measure trace gas concentrations within the plasma environment non-intrusively. Both the plasma formation and the CRDS laser can be triggered and synchronized to ensure temporal overlap between the optical probe and the plasma discharge.

1.5 Dielectric Barrier Discharge (DBD) Reactors

A dielectric barrier discharge (DBD) is a class of non-equilibrium gas discharge defined by the presence of an insulating dielectric material between electrodes covering one or both electrode surfaces [26]. The utilization of a dielectric material such as quartz or ceramic limits the discharge current, preventing direct free flow of electric current. A dielectric barrier discharge requires alternating voltages, or a pulsed discharge to operate [26]. A dielectric material such as quartz effectively prevents the flow of direct current (DC). Charges accumulate on the surface of the dielectric material instead of conducting current. While direct current is blocked by the insulator, alternating current couples across the dielectric barrier through the oscillating electric field [26], [27], [28]. This creates a buildup of surface charges on the dielectric walls, which store energy and regulate the discharge intensity. The dielectric material acts as a capacitive ballast; charge accumulation on the dielectric surface induces an electric field that opposes the electric field of the supplied AC current [27]. The induced reverse electric field opposes the applied voltage, creating a limit to the amount of energy that can be deposited into the gas to form a plasma. This limiting principle is what allows a dielectric barrier discharge reactor to maintain a nonthermal equilibrium. Maintaining nonthermal equilibrium is crucial to preventing thermal arcing [26], [27].

A visually homogeneous plasma formed within a dielectric barrier discharge consists of a large number transient, filamentary channels known as microdischarges [26]. Microdischarges are short lived and have an average radius of 100 um. The initiation of localized microdischarge channels occurs once the magnitude of the applied electric field surpasses the critical breakdown threshold of the gas. Electron avalanches occur when a significant charge is built up on the dielectric materials surface to overcome the resistance of the gas [26]. The process of electron avalanche occurs when a primary energetic electron impacts background gas molecules, ionizing them and generating an exponentially growing number of charge carriers [29]. The dense cloud of charged particles formed by an electron avalanche is referred to as a space charge. The electron avalanche is sped up by the electric field induced by the space charge, allowing a self-propagating streamer to form that can move faster than a single free electron. The high energy at the tip of the self-propagating streamer is able to form a conductive path for electrons. A cathode fall layer is formed when the ionization wave (streamer), enhanced by space-charge effects, propagates back from the anode to the cathode. Upon bridging the gap, this layer establishes a high local electric field that facilitates secondary electron emission, thereby initiating the high-current phase of the microdischarge [26], [27]. According to the literature, the surface charge deposited by a single microdischarge spreads laterally, covering an area significantly larger than the diameter of the discharge channel itself. This wide distribution creates a localized zone of reduced electric field where the voltage is insufficient to sustain ionization. The space charge dissipates and the flow of current terminates, effectively extinguishing the discharge pathway [26]. As the supplied voltage continues to rise, new discharge pathways are forced to avoid the areas of low electric field by striking in the surrounding areas outside the surface charge area of another microdischarge. Reducing the local electric field around a microdischarge limits the amount of current that can dissipate through a given streamer avoiding a thermal arc, but evenly distributes the microdischarges across the electrodes creating a visually homogeneous plasma [26].

A dielectric barrier increases the energy of electrons while keeping the average temperature of the gas close to that of the ambient environment, characterizing the system as a non-thermal or “cold” plasma [30]. A dielectric cylinder barrier excites free electrons, and cause a cascade of electron impacts that spread though out the gas present within the reactor, forming radicals and molecular species not originally within the gas [30].

1.6 Research Objectives and Thesis Outline

The goal of this research project is to find a more efficient reformation process to maximize H_2 production pre-combustion or pre-fuel cell would lower the price of hydrogen fuel to power vehicles and power plants. A reduced cost means a lower barrier of entry into the green fuel economy, allowing consumers, companies, and countries with low capital to reduce their carbon footprint.

This research aims to bridge the gap ammonia storage and combustion. While ammonia and hydrogen are not currently viable to sustain a substantial percentage of global power demand, infrastructure exists to make it a viable alternative energy source. Facilities are in place that produce ammonia in copious quantities, and ICE's and fuel cells are prepared to utilize hydrogen. Hydrogen powered vehicles are restricted by the cost to transport, produce, and store pure hydrogen.

The inefficiency of converting ammonia to hydrogen hinders ammonia's integration as a hydrogen fuel carrier and remains the largest missing component of ammonia integration. Utilizing a non-intrusive measurement technique such as Cavity Ring-down Spectroscopy (CRDS), the reformation process of ammonia can be maximized for combustion efficiency.

The goal of this thesis is to present an in-situ measurement of NH_2 within a nanosecond pulsed plasma reactor using CRDS. This overarching objective will be achieved via the following specific objectives.

- Design and manufacturing of plasma reactor
- implementation and testing of gas flow and plasma systems
- implementation and testing of CRDS diagnostic systems
- preliminary detection of the NH_2 radical within the reactor

- parametric studies of plasma conditions effect on NH_2 concentrations

The layout of the remainder of this paper is as follows: Chapter 2 provides a literature review of related topics, Chapter 3 describes the experimental setup, Chapter 4 contains the results and discussions, and Chapter 5 contains conclusion and future work.

CHAPTER 2

Review of Cavity Ring-Down Spectroscopy and NH_2 Spectroscopy

2.1 Spectroscopy

Spectroscopy characterizes the physical properties of matter by analyzing its response to electromagnetic energy, typically through absorption, emission, or scattering processes [31]. A spectrum is a plot of data collected using spectroscopy across a frequency or wavelength range. A spectrum is typically represented as an emission or absorption spectrum. A continuous spectrum consists of a band of electromagnetic radiation across a specific range of frequency or wavelength that is unbroken for the entire range. Spectroscopic data is generally represented as intensity plotted against frequency or wavelength [31]. An emission spectrum consists of bright lines or bands representing the energy released by excited species returning to lower energy states. Conversely, an absorption spectrum is defined by a reduction in intensity at specific wavelengths, appearing as gaps in a continuous spectrum, corresponding to photon energy absorbed by the sample. Both absorption and emission spectra are examples of discrete spectra [31]. An example of an emission and absorption spectrum are shown in figure 2.

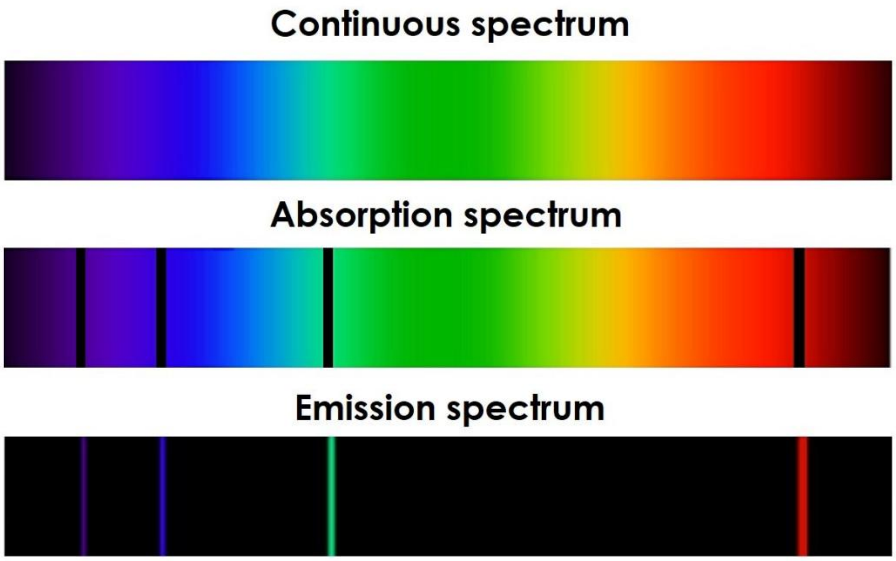

Figure 2: Example of continuous, absorption, and emission spectra [32]

Spectroscopy is a powerful tool that can provide detailed insight into the physicochemical properties of the compound being studied. The intensity and location of emission and or absorption lines can provide information such as material composition, temperature, ground and excited state populations and specifically for this work, species concentrations [32]. In all methods of spectroscopy, an electromagnetic radiation source directed at the sample under investigation. This electromagnetic radiation source can be naturally occurring, or experimentally designed. Most standard spectroscopy methods involve a spectrograph, a device capable of recording the frequency, linewidth, and wavelength of the spectral signal by passing the collected light through a slit onto a prism, separating the light into bands.

In some cases, the full spectra are not required to extract the required data. Some methods of spectroscopy probe specific absorption or emission spectra. This can be achieved with specific lamps, or lasers. A laser can be used to target a specific transition of the sample being studied. By targeting a known absorption feature with a given wavelength, a laser outputting the same wavelength can be directed at the studied sample. By absorbing energy, an electron moves from a ground state to an excited state. When the electron returns to a ground state following excitation, the energy is released via non-radiative decay (heat) or electromagnetic radiation (light). From this excitation principle, the two main spectroscopy studies can be performed, emission and absorption. The emission of electromagnetic radiation as the electron returns to ground state can be analyzed, or the amount of energy absorbed by the sample can be measured. The latter principle forms the basis Cavity Ring-down Spectroscopy (CRDS), the primary diagnostic technique employed in this thesis. Absorption spectroscopy requires a pulsed laser source to quantify the energy of each pulse, allowing for the determination of the energy difference with and without the experimental sample present.

2.2 Cavity Ring-Down Spectroscopy (CRDS)

Cavity ring-down spectroscopy is a highly sensitive laser-based absorption technique that has been reviewed in the literature [33], [34]. In CRDS, the absorbing sample (NH_2 containing plasma in our case) is housed within a high-finesse optical cavity typically formed from a pair of high-reflectivity mirrors. The laser beam is coupled into the cavity and passes back-and-forth many times between its mirrors. Upon each reflection at the rear cavity-mirror, a small fraction of the beam leaks out to a photodetector measuring the light decay within the optical cavity. With no absorber present (or the laser detuned from the absorption) the cavity decays primarily owing to mirror loss. When the laser light is resonant with absorption of the sample then the decay is hastened. The change in decay rates may be found from the change in ring-down signals and then used to determine the sample's absorbance and concentration. The technique affords high sensitivity owing to a combination of long effective path length and insensitivity to laser energy fluctuations. Under appropriate conditions, the ring-down signal $S(t, \nu)$ decays (single-) exponentially versus time as[35]:

$$S(t,\nu) = S_0 exp\left(^{-t}/_{\tau(\nu)}\right) \quad ; \quad ^1/_{\tau(\nu)} = \frac{c}{l}[\int k(x,\nu)dx + (1-R)] \tag{1}$$

where τ is the 1/e time of the decay (termed the ring-down time), c is the speed of light, l is the cavity length, k (ν,x) is the absorption coefficient, ν is the laser frequency, x is the position along the beam in the cavity, and 1-R is the effective mirror loss (including scattering and all cavity losses. If the absorber is uniformly present over a column, as we assume here, then the integral over length can be replaced with the product $k(\nu) \cdot l$.

As in conventional absorption, the absorption coefficient should be convolved with the laser lineshape. In practice, the measured ring-down signal is fitted with an exponential, and the ring-down time τ is extracted. Combining τ with the "empty cavity ring-down time", τ_0 (which in practice is measured by detuning the laser) allows determination of the sample absorbance:

$$Absorbance(\nu) \equiv k(\nu) \cdot l = \frac{l}{c}\left[\frac{1}{\tau} - \frac{1}{\tau_0}\right] \tag{2}$$

A widely used method to infer species densities is to scan the laser frequency across the absorption line and to measure the frequency-integrated absorption spectrum) $\int Absorbance(\nu)d\nu$,i.e., the "line area". The rationale is to remove lineshape dependences.

Practically, a tau, or ringdown time, is width of the signal at 1/e the height of the exponential decay of the voltage signal (figure 3).

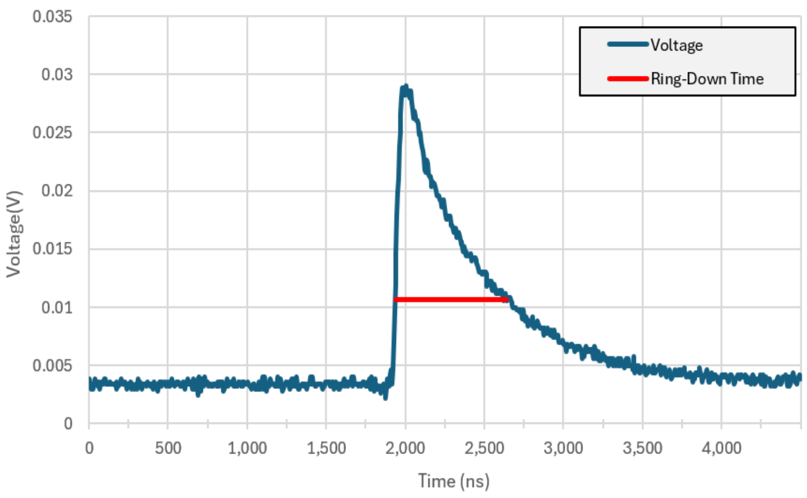

Figure 3: A CRDS signal, with the tau or ringdown time labeled.

This signal is recorded and processed constantly while a narrow linewidth adjustable wavelength laser such as a dye laser is continuously scanned across a wavelength range. The value of tau will decrease when the wavelength of the laser corresponds to a wavelength that the sample within the cavity absorbs to reach an excited state. The values of tau are then plotted vs. wavelength. Instead of dark lines, or gaps in the spectrum that we see in absorption spectra plots like in figure 1(the one from the spectroscopy section). Instead, we get a much more detailed idea of the linewidth and intensity of a feature. As the laser wavelength approaches the center of the feature, the value of tau gradually decreases, and begins to increase again as the wavelength moves past the center of the feature. An example of a spectroscopic scan measured using cavity ring down spectroscopy is shown in figure x. The value of tau is at a maximum when no energy from the laser is absorbed by the sample. This occurs when the wavelength of the laser does not match with any of the absorption wavelengths. This provides information required to determine the population of the transition, and the density of the measured species.

2.3 NH_2 Density Calculations

Determining NH_2 densities requires calculations of the rotational and vibrational partition functions $Q_r \; and \; Q_v$ and the Boltzmann Fraction f_b [12]. These parameters describe the fractional population of the overall population that is in the measured state including temperature dependence. The Rotational partition function is given as:

$$Q_r = \frac{\sqrt{\pi}}{\sigma}\sqrt{\frac{8\pi^2 I_A k T_{rot}}{h^2}}\sqrt{\frac{8\pi^2 I_B k T_{rot}}{h^2}}\sqrt{\frac{8\pi^2 I_C k T_{rot}}{h^2}}$$

where σ is the symmetry number, I_i are Moments of Inertia, k is the Boltzmann constant, T_{rot} is rotational temperature (in Kelvin), and h is Planck's Constant. $\sigma = 2,\; I_A = 1.178 \times 10^{-40} gcm^2,$ $I_B = 2.126 \times 10^{-40} gcm^2,\quad I_C = 3.425 \times 10^{-40} gcm^2,\; k = 1.381 \times 10^{-16}\, {}^{erg}/_{K}$, and $h =$ $6.626 \times 10^{-27} ergs$. The vibrational partition function is defined as:

$$Q_v = \prod_{i=3}^{3}\left(\frac{e^{\left(-\frac{hcw_i}{2kT_{vib}}\right)}}{1 - e^{\left(-\frac{hcw_i}{2kT_{vib}}\right)}}\right)$$

where w_i are vibrational frequencies, and T_{vib} is vibrational temperature. $\omega_1 = 3219\; cm^{-1}, \omega_2 =$ $1499\; cm^{-1}$, and $\omega_3 = 3301\; cm^{-1}$. Rotational and vibrational partial functions are used to calculate the Boltzmann fraction which is defined as:

$$f_b = \frac{3}{4}\frac{(2J^{"} + 1)\, e^{\left(-hc\frac{w_1}{2kT}\right)} e^{\left(-hc\frac{w_2}{2kT}\right)} e^{\left(-hc\frac{w_3}{2kT}\right)}}{g^{"} Q_r Q_V} e^{\frac{-e_{rot}hc}{kT_{rot}}}$$

where $J^{"}$ is the lower state rotational quantum number, $g^{"}$ is the lower state degeneracy, and e_{rot} is the rotational energy of the lower state. $J^{"} = 3,\; g^{"} = 3,$ and $e_{rot} = 43.1 cm^{-1}$. This formulation explicitly includes the vibrational zero-point energy (which some studies neglect). The Boltzmann fraction is key spectroscopic value to determining density of a molecule. The density equation of NH_2 is defined as:

$$n_{NH_2} = \frac{A_{int,\ frequency}c}{\sigma_{int}f_b}$$

where $A_{int,\ frequency}$ is the integrated absorption in terms of frequency collected from experimental data (units of cm^{-2}), c is again the speed of light (cm/s), and σ_{int} is the integrated absorption cross-section of the known lineshape of NH_2 at the frequency of study. This integrated absorption cross-section is crucial to determining NH_2 concentrations. Due to a lack of NH_2 absorption studies in literature, only densities of NH_2 in at 16,739.9 cm^{-1} can be determined [12]. The value of σ_{int} at 16,739.9 cm^{-1} is $2.21 \times 10^{-6} cm^2 Hz$.

2.4 Spectroscopy of the NH_2 Radical

The amino radical NH_2 is an asymmetric top molecule that plays a critical role as a key indicator to the efficiency of ammonia combustion and plasma decomposition kinetics [17]. NH_2 spectroscopic studies have primarily focused on $\tilde{A}^2A_1 \leftarrow \tilde{X}^2B_1$ transition systems. This transition is characterized by strong absorption spectrum across the visible wavelength range of 400 to 900 nm [36]. These large absorption cross-sections make this transition an optimal selection for high-sensitivity detection [36], [37].

The electronic transition $\tilde{A}^2A_1 \leftarrow \tilde{X}^2B_1$ is characterized as the excitation of an electron from the ground state $\tilde{X}^2B_1$ to the first excited state $\tilde{A}^2A_1$.

2.5 Gaps in Current Literature

Faingold et al. have developed comprehensive kinetic model solvers to determine the ammonia and oxidizer ignition characteristics in plasma simulation [11]. Simulations investigated the influence of varying voltage pulse characteristics. With higher PRF, ammonia ignition temperature decreases as seen in Figure 4.

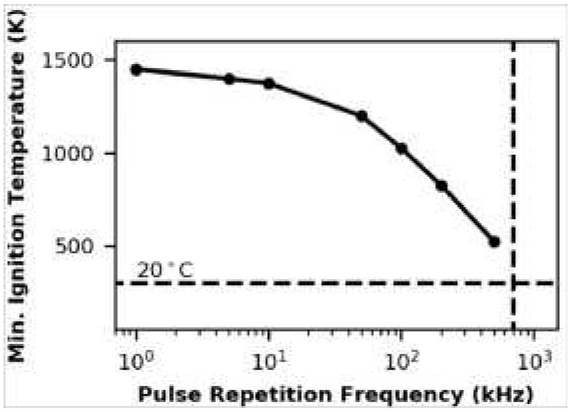

Figure 4: Minimal Ignition temperature of ammonia vs PRF [11]

These findings demonstrate the potential of non-thermal plasma to mitigate thermal runaway and enable stable decomposition at a wide range of temperatures [11]. Operating at lower temperatures facilitates a stable reformation process and promotes the complete dissociation of ammonia into reformate species. This, in turn, optimizes the combustion of the reformed ammonia mixture by increasing NH_2 concentrations, thereby reducing the NO_x emissions and enhancing H_2O and H_2 yields [12].

Faingold et al. in a subsequent study utilized advanced kinetic models and chemistry model solvers to better utilize plasma to optimize the ignition of an ammonia-air mixture [2]. Simulations varying the PRF revealed that increasing the frequency decreased the ignition delay and affected the initial concentrations of both H_2 and NH_2 as seen in Figure 5.

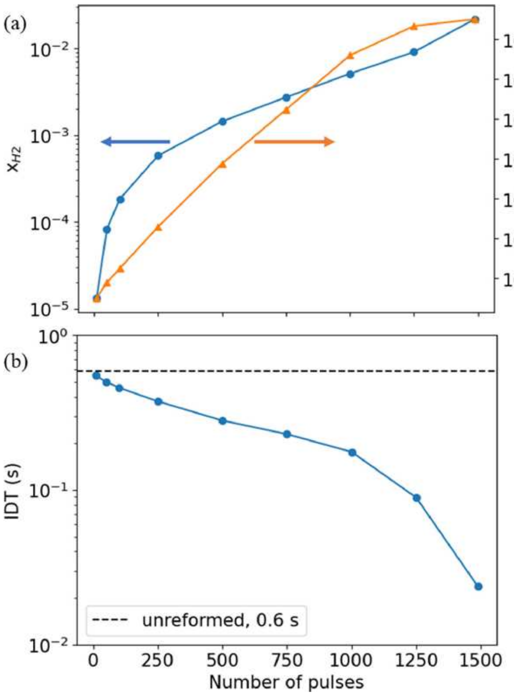

Figure 5a- Concentrations of H2 in yellow, NH_2 in blue, 5b- ignition delay. Both plots are vs. Number of pulses [2]

Similar experiments and simulations carried out in [19] demonstrate a direct relationship between the specific energy input (SEI) and the amount of NH_3 reformed into hydrogen. (SEI) is defined as the ratio of plasma power to the total fuel flow rate [19]. Increasing SEI can directly increase the amount of H_2 produced as shown in figure 5.

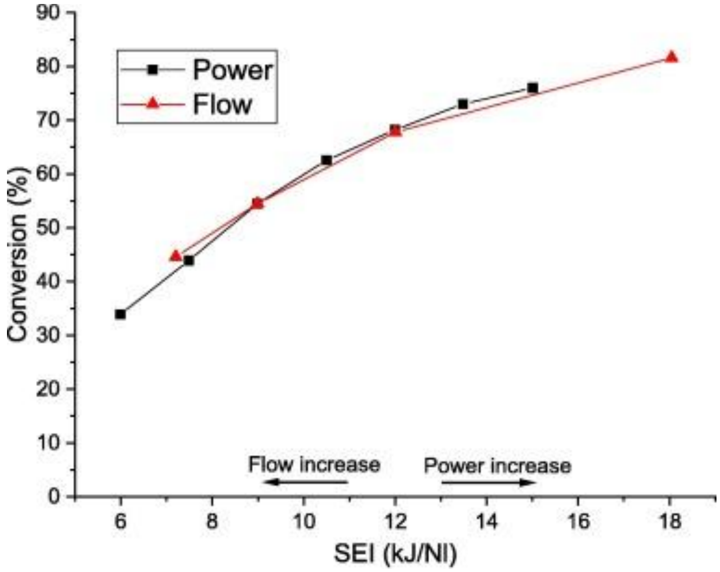

Figure 6: SEI vs. percent of converted ammonia [19]

CHAPTER 3

EXPERIMENTAL SETUP AND DIAGNOSTICS

3.1 Design and implementation

The plasma reactor was designed to facilitate in-situ CRDS measurements within a DBD reactor. Typical DBD reactors have a solid electrode, completely wrapping around the dielectric material. This reactor utilizes a mesh outer electrode with large openings to allow for visual access to the plasma discharge formed within the chamber.

3.2 Nanosecond Pulsed Plasma Reactor Design

The ammonia plasma reformer is depicted in figure 2. The reactor interfaces with three main systems. Gas delivery, high-voltage, and the CRDS diagnostic. The reactor's main body is composed of MACOR ceramic endplates and a quartz cylinder with an outer diameter of 55 mm and a material thickness of 3.84 mm forming a chamber volume of 0.486 L. Machinable ceramics such as MACOR not only maintain insulative properties, but allow for direct integration of subsystems within the end-plates, thereby minimizing the experimental footprint. The ceramic endplates have machined grooves that seat the quartz cylinder against O-rings, allowing for the walls to be aligned under vacuum, sealing by differential compression.

3.2 Gas Flow and Control System

The gas flow system is comprised of a 50 lb tank of %99.999 research-grade anhydrous ammonia supplied by Airgas. All gas feedline within the system utilizes ¼ in stainless steel tubing with 0.18 in inner diameter and ¼ in SWAGELOK fittings, with the exception of the gas feed tubing that passes through the faraday cage to the reactor. To prevent arcing within the faraday cage, ¼ in polyethylene tubing was used to facilitate ingress and egress of ammonia from the faraday cage. Flow rate is controlled by an Alborg (P11S5-EA0), (044-40-GL-EA) rotameter pre reactor. The polypropylene tubes connect to Swagelok fitting on PEEK plastic adapters that thread directly into the MACOR ceramic endplates. These fittings are corrosion resistant, as well as being poor conductors of electricity. In addition, these PEEK fittings thread straight into the MACOR ceramic endplates and allow for gas to evenly flow along the length of the reactor to promote mixing and uniform dissociation. Post reactor external of the faraday cage, reactor pressure is controlled by a precision needle valve before the NAVAC NP12AD1 vacuum pump. After the needle valve and before the NAVAC vacuum pump, a digital pressure gauge (OMEGA: DPG409) is installed. This setup allows for precise control of the flowrate and pressure within the ammonia plasma reformer to achieve desired conditions for a variety of parametric studies.

3.3 High-Voltage Pulse Generation

The high voltage electrodes on the reactor consist of an outer copper electrode with a diameter of 62.21 mm, a width of 65.41 mm, and a material thickness of 1.09 mm. The outer copper electrode is wrapped tightly around the quartz tube to create a uniform positively charged electrode. The inner ground electrode has a diameter of 1.59 mm and is surrounded by a ceramic sheath with an outer diameter of 3.18 mm. The inner electrode is positioned within the reactor such that it is concentric with the quartz cylinder and outer copper electrode, effectively forming the dielectric cylinder barrier reactors core mechanism. The reactor is fully shielded and ground to a double walled faraday cage comprised of both copper and brass mesh walls. The floor of the faraday cage is 1/8th inch stainless steel sheet metal, and all large gaps of the faraday cage were sealed using conductive copper tape. The entire faraday cage was insulated from the stainless-steel optical table to prevent the formation of a secondary ground path. When the faraday cage is grounded to the table, current and voltage reflections are observed with probes, and the table effectively becomes an antenna, outputting EM noise and distorting the signal picked up by the PMT.

The reactor plasma formation is controlled by an external high voltage pulser system comprised of three main components. A high-voltage nano-second pulse generator (TPS SSPG-20X-100K) supplies the high voltage bursts and is powered by a DC power supply (Magna-Power SL500-3/UI+LXI). The pulse generator is triggered by a waveform generator (Agilent 33150A), which is used to set the number of pulses and their frequency. The high voltage pulses are sent to the reactor via a shielded coaxial cable, where the shielding is grounded to both the pulse generator's body, and the faraday cage. Once within the cage, the coax cable is split and sent to its respective terminals on the plasma reactor.

3.4 Laser and Optical Setup

The optical cavity used to perform CRDS within the chamber of the plasma reactor is formed by two HR mirrors mounted in the MACOR ceramic endplates. The HR mirrors in this study are centered at 610 nm and have a reflectivity of %99.9997. The probing beam is formed by a frequency doubled Nd:YAG laser (Continuum, Powerlite Precision II 8000) outputting a 532 nm beam at 10 Hz with a pulse energy of 15 mJ. The pump laser pumps a tunable dye laser (Sirah, Cobra-Stretch). The tuneable dye laser utilized Rhodamine B dye to achieve the desired wavelength to probe the $\tilde{A}^2A_1(0,10,0) \leftarrow \tilde{X}^2B_1(0,0,0)$ transition. The dye laser has a frequency of 10 Hz with an energy of 0.5 mJ. The beam is then steered by eight protected silver mirrors (Thorlabs: PF10-03-P01) and raised vertically using a periscope. A series of irises are used to maintain a clean beam profile entering the HR cavity. The HR mirrors are spaced 6.64 cm apart. The light is then steered by more protected silver mirrors and collected using a photo multiplier tube (PMT) (Tube:R9110, Socket:E71763). The PMT is fitted with a 600 nm Bandpass filter with a 10 nm FWHM (ThorLabs:FB600-40) to ensure that only light within the desired spectral region is being analyzed.

The last two steering mirrors before the optical cavity are used to adjust the angle and level of the probing beam. Special targets were designed to mount in place of the HR mirrors to ensure that the beam was completely concentric to both the entrance and the exit of the optical cavity. When the beam is properly aligned to the optical cavity, the cross hairs of the target will align perfectly as seen in figure 7.

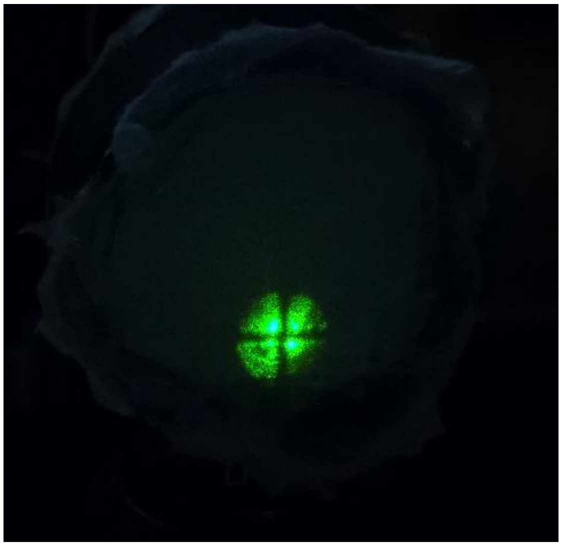

Figure 7: A well aligned cavity using proprietary targets

When misaligned, the lines will be uneven thicknesses, or extra lines will be visible.

3.4.1 Cavity Ring-Down Spectroscopy (CRDS) Acquisition System

To control the output wavelength of the probing beam, the Sirah 2.6 software is used. With a spectral linewidth of 0.03 picometers, the wavelength of the dye laser can be scanned over a region of interest to measure absorption. To record the absorption feature measured, a proprietary LabVIEW program is used to capture the ringdown signals for every picometer scanned, allowing for the recording of high-resolution spectroscopic plots. The LabVIEW program takes the incoming voltage signal from the RIGOL oscilloscope which plotted the voltage signal output by the PMT. The voltage signal is of the decay of light within the HR cavity, or the ringdown signal. The rate of decay of light within the chamber is indicative of the concentration of the sample in the HR cavity. The tau is determined by taking the width of the signal at 1/e the height of the maximum intensity as recorded by the LabVIEW. The decay curve as recorded by the LabVIEW program is shown in figure x. CRDS theory is based on single mode exponential decay of light within the cavity. A semi-log plot is utilized to confirm that the decay of the measured signal is an exponential decay. The semi-log plot is the natural log of the voltage plotted against time. For a perfect exponential decay, the semi-log plot is a straight line with an R^2 value of 1. To have a perfect exponential decay, zero ambient light after the HR cavity would be allowed into the detector, and no electromagnetic noise can be present within the testing environment. Thus, a perfect exponential decay is nearly impossible in an experimental setting, especially one that utilizes a HV pulser to ionize the measured sample. However, the effect of this signal contamination can be minimized by enclosing the beam path with black fabrics and anti-reflective materials to block light, and a faraday cage to shield the plasma source to prevent the detection of EM noise. To further filter out this noise, a 90-10 fit is implemented. A 90-10 fit in this experiment refers to the range of the exponential decay, meaning that 90 to 10 percent of the decay is determined to be exponential. This region is selected, because the first 10 percent of the decay can be affected by light contamination, while the last 10 percent can be affected by electromagnetic noise. This 90-10 fit is the region that is analyzed by the semi-log plot.

The tau, or ringdown time is then determined from only the region that is exponential, because the main principal of CRDS is the characterization of an exponential decay. The tau is then plotted in a spectroscopic plot of tau vs. shot number, with each shot number corresponding to a particular wavelength that the dye laser is centered at for a given shot. For simplicity, I will simply refer to this plot containing tau vs. wavelength, skipping the intermediate step of assigning wavelength in post processing. The spectroscopic plot directly visualizes the absorption of a feature. The wavelength scan range of the dye laser must be selected to completely include the feature of study, and significant room on either side of the feature. As the wavelength scans across a region where no absorption is present, our tau is at its maximum. As an absorption approaches, the tau value will decrease with increased wavelength. As the scan passes through the center of the absorption feature, the tau values will decrease with wavelength. This creates a dip, as seen in figure x. It is very important that the scan includes a stable, clean baseline value to accurately determine the change in tau. The scan must include ample room on either side of the feature to ensure that the tau 0, or baseline tau on either side of the feature is the same. It is possible for the HR mirrors to drift, causing the Tau values over the scan to decrease such that the baseline tau is much lower after the feature than before. However, this drift rate can still be accounted for as its rate of change is constant and can be linearized to negate the slope.

The LabVIEW program then outputs an excel file containing all of the tau values and wavelengths for post processing. The LabVIEW also outputs each voltage decay signal it collects. This allows for the fitting of the decay, creation of a semi-log plot, and creation of a spectroscopic plot independent from LabVIEW. Allowing for the data to processed and plotted using programs like MATLAB allow for more plot customization, and the testing of different fitting methods and their effect on the semi-log or tau values. Since MATLAB is already used in post processing for calculating integrated absorption and NH_2 densities, including the post processing done by LabVIEW into the MATLAB acts as an accuracy check for LabVIEW and keeps all the post processing in one place.

The Sirah 2.6 dye laser control software and LabVIEW did not communicate with each other, so the LabVIEW software could not detect when the wavelength scan began, what wavelength region is being probed, or what wavelength the laser is currently at. Thus, manual calibration of the data was required. The current wavelength of the dye laser is recorded with the current tau value measured with the LabVIEW. This is done at many points across the scan, and linearly interpolated since both the LabVIEW and dye laser have fixed scan and record rates.

The most important variables in the acquisition system are the scan rate of the dye laser, and the averaging of the voltage signals by the oscilloscope and LabVIEW. These variables directly affect the resolution of the absorption feature scanned. If averaging was set to zero, the scan rate of the laser can be fast, as the response time of the signal is only determined by the ringdown time of light within the cavity. Since the laser cannot scan that quickly, any scan rate would work. However, since there is slight variation in tau values for every shot of the laser, an averaging of tau values is required. This can lead to prolong exposure time for each wavelength position. Therefore, a scan rate of the laser must be selected such that the lab view can record at least one decay signal per shift the dye lasers wavelength. It is better to have more data points recorded per wavelength shift than needed as they can be averaged out later in post processing. While all averaging could be done post processing, averaging during collection allows for better visualization and recognition of an absorption feature with a human eye, and significantly decreases the amount of data collected if averaged live. Single feature scans of most features could be achieved in as little as 3 minutes, while full sub band scans across 5 nm took over 2 hours.

For the voltage study, the transition in this wavelength region was probed 0.08 ms after the formation of the plasma, from supplied voltages ranging from 400 to 950 VDC. For the transient study, the transition was probed from 0.08 ms to 30 .08 ms after the pulse with a supplied voltage of 800 VDC. The timing is shown below in figure 2. A wavelength range is specified as 597.355 to 597.41 nm, with a scan rate of 0.03 nm per minute.

3.5 System Synchronization and Timing

Synchronization of the diagnostic system with the plasma system is governed by the Q-switch fixed sync output of the Nd:YAG pump laser, which functions as the master timing clock of the system. To ensure thermal equilibrium and pulse energy stability, the laser flashlamps and Q-switch operate continuously at a fundamental repetition rate of 10 Hz. Since laser emission occurs simultaneously with the Q-switch trigger, the laser pulse cannot probe the plasma discharge initiated from its own trigger signal. Since the plasma generation consists of nanosecond-duration pulses while the optical probing occurs on a millisecond timeframe, precise synchronization is necessary to ensure the CRDS measurement captures the correct post-discharge environment.

Q-switch triggered the delay generator which triggered the waveform generator. This delay was to close the gap in the pulse train because the system operated in burst mode, as the HV pulser could not sustain 10 kHz for an entire period. The delay generator delayed the formation of the plasma such that the laser could probe the previous burst. The waveform generator sent a trigger signal to the HV pulser.

CHAPTER 4

RESULTS AND DISCUSSION

4.1 Plasma discharge validation

Integration of the HV pulser system into the plasma reformer setup required confirmation of its function, and ability to meet the power and frequency requirements to adequately decompose ammonia within the reactor. Initial testing of the pulser's capabilities were carried out using a pin to pin testing configuration at atmospheric conditions (figure 8).

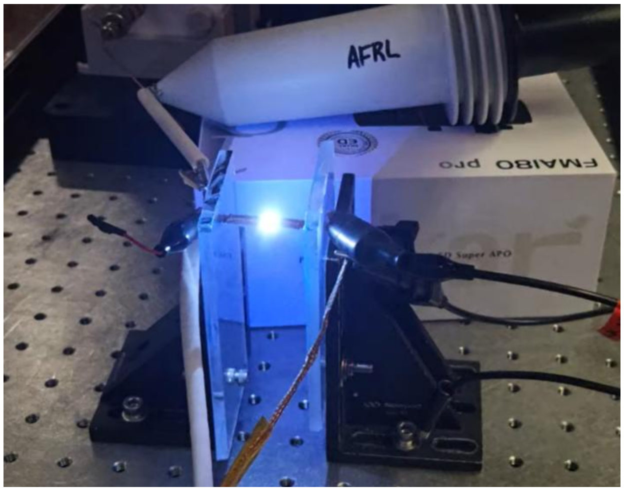

Figure 8: Plasma discharge at atmospheric conditions to validate function of HV pulser system

This initial test validated that the pulser system had arrived in functioning condition from loan from the AFRL. This confirmation gave confidence that the pulser system was ready to be tested with the reactor, and that if any problems were to arise, it would be due to integration into the new system.

During preliminary reactor testing with the high-voltage pulser, irregular discharges that did not have a stable frequency were observed when the pulsers triggering signal was set to high pulse repetition frequencies or high supplied voltages. A uniform plasma discharge was formed in both an argon and air-filled reactor chamber at vacuum pressures below 0.8 PSIA. The plasma discharge was continuous at supplied voltages in the range 400-600 VDC, when the pulser was triggered at a frequency of 10 KHz, a pulse width of 1.5 μs, and an edge time of 5 ns. These parameters created the desired plasma characteristics (figure 3).

Increasing PRF caused the pulser to overdraw current, and as a result, plasma was formed in bursts, with discharges only lasting for 500 ms. While plasma was visible below supplied voltages of 400 VDC, the plasma was not homogenous in nature. Manipulating parameters to the values resulted in suboptimal plasma discharges and low SEI and will be avoided for the remainder of this experiment.

4.1.1 Plasma Characterization

To confirm the desired plasma conditions were met, voltage and current measurements were conducted to determine the SEI of the plasma within the reactor. The plasma discharge was continuous at supplied voltages in the range 400-600 VDC, when the pulser was triggered at a frequency of 10 kHz. Higher pulse repetition frequency (PRF) led to excessive current draw from the high voltage pulser, resulting in pulsed plasma formation with pulse train discharge durations limited to 500 ms. Supplied voltages up to 950 VDC were achieved when the pulse train duration was set to 400 ms. This allows for testing of higher SEI cases for parametric studies. Figure 9 illustrates how the ammonia plasma formed within the reactor appears to the human eye.

Fig. 9: Photograph in real colors of the anhydrous ammonia plasma.

The waveforms corresponding to the flow conditions investigated in this paper are shown in **Fig.** . The peak voltage of the incident pulse is recorded at 5.9 kV with a full-width at half maximum of 15 ns. The current and voltage waveforms are synchronized using the purely capacitive behavior of the reactor filled with air at atmospheric pressure, as explained in [38]. The electric energy deposited in the plasma is inferred from the integral of the product of the voltage and current waveforms and is approximately 0.3 mJ/pulse.

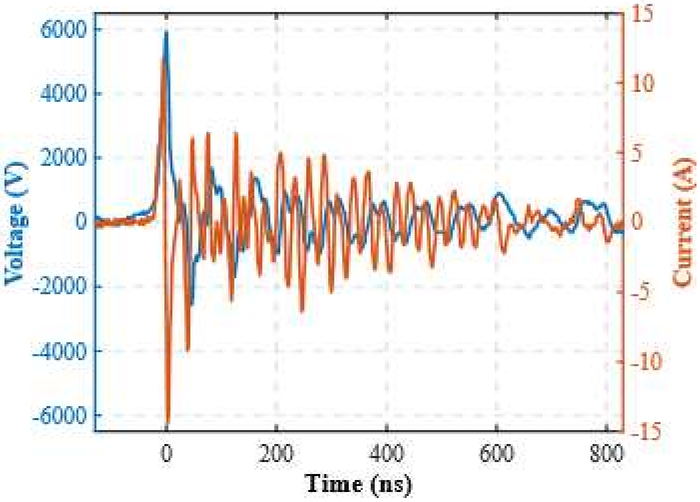

Fig. 10: Voltage and current waveforms for the ammonia plasma.

Two plasma regimes exist within the reactor at varied SEI. At low SEI a corona is the dominant discharge formation around the center ground electrode that does not completely fill the volume of the reactor chamber (figure 11). Because ammonia dissociation is caused by the collision of high energy electrons, the corona discharge causes disassociation primarily around the ground electrode, out of the path of the probing laser beam. This limits detection of NH_2 in this low energy regime.

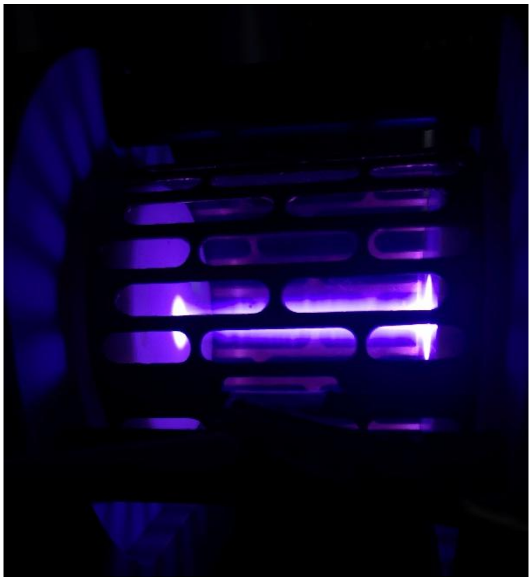

Figure 11: Color image of Corona (low volume) discharge at 22% NH3/78% N2 45.1 SLPM 10 kHz, 100 pulses 600 VDC, 0.07 SEI

DBD (high volume) is the second plasma regime that is formed when high energy is deposited into the plasma (figure 12).

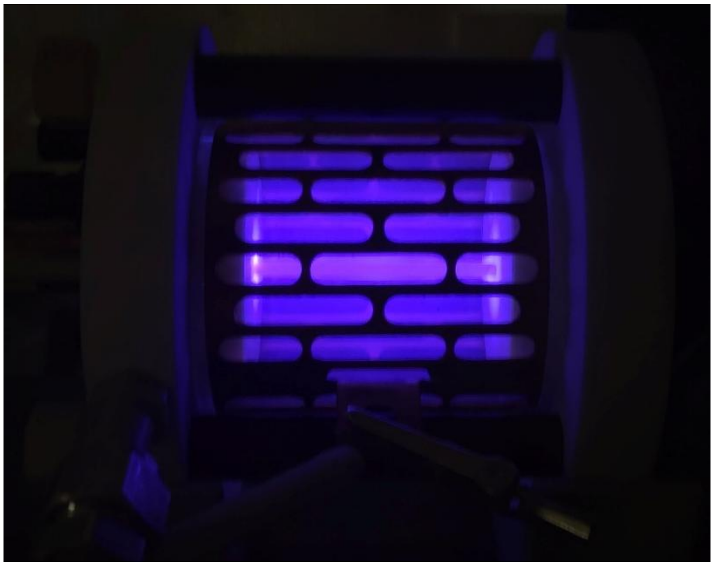

Figure 12: DBD regime at 22% NH_3/78% N_2 45.1 SLPM 100 kHz, 100 pulses 900 VDC, 0.49 SEI

By plotting supplied voltages VS. SEI/EPP/peak voltage, a clear link, trend, change can be seen. For all plots, a supply voltage of 600 VDC or less results in significantly lower SEI/EPP, with a massive difference observed in the measured peak voltage across the electrodes of the reactor (figure 13).

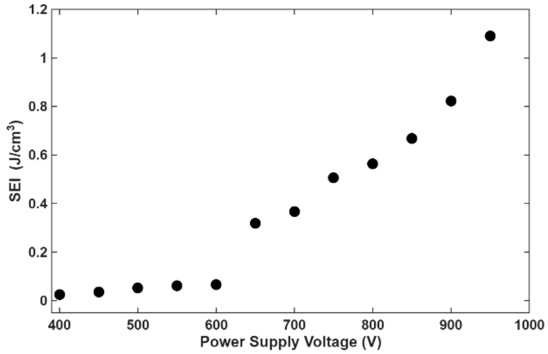

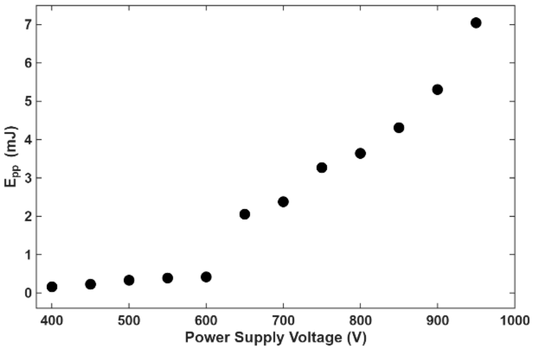

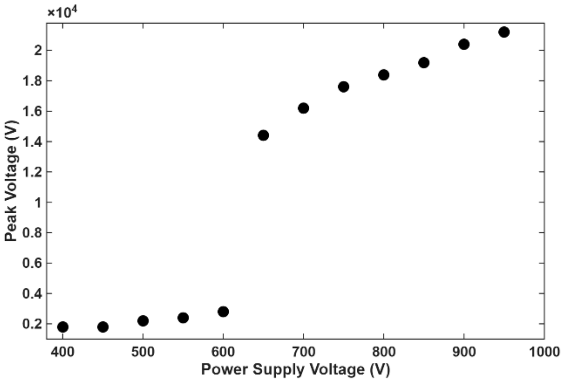

Figure 13: DC power supply voltage vs. SEI, EPP, and peak voltage.

The plots in figure 9 quantify the difference between the two visually observed plasma regimes within the reactor. To achieve a homogenous discharge in the DBD regime for our reactor setup, a supply voltage of 650 VDC or greater is required. A reactor with a full volumetric discharge is optimal for maximizing ammonia dissociation. Characterizing the two observed plasma regimes within the reactor is crucial to optimization of the reactor and determining optimal voltages. The issue with the corona discharge is that the visual glow occurs out of the CRDS path. While NH_2 can still be detected when the plasma is in the corona regime, a majoring of the concentration will be close to the corona formed around the anode. Because of the change in trends in all three plots, using SEI to quantify changes in NH_2 density provides results that do not have clear trends. As a result, the plotting of relative and actual NH_2 densities in the power study are plotted against supplied voltages. While this does not allow for direct comparison of the plasma source, it provides the clearest trend between increased energy and NH_2 densities.

4.2 Preliminary NH_2 detection

The e sub-band of the $\tilde{A}^2A_1(0,10,0) \leftarrow \tilde{X}^2B_1(0,0,0)$ transition, shown in figure 14a below, is the standard for NH_2 spectroscopy; however, hardware limitations delayed our study of this absorption feature until appropriate 600 nm optics were acquired [36].

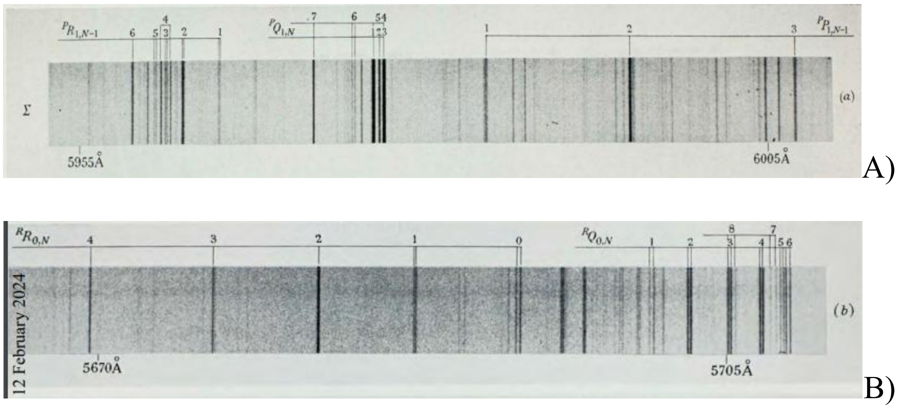

Figure 14: a) shows the E band, and b) shows the pi band [36]

Our first set up utilized HR mirrors and a dye laser configured for probing the 560 nm region, so our preliminary detections of NH2 were done on the $\tilde{A}^2A_1(0{,}10{,}0) \leftarrow \tilde{X}^2B_1(0{,}0{,}0)$. While gaps in literature exist, preventing conclusive NH2 density calculations, a relative density can be determined, and a estimated actual density can be determined by correlating the absorption of transitions within the $\tilde{A}^2A_1(0{,}9{,}0) \leftarrow \tilde{X}^2B_1(0{,}0{,}0)$ band.

During this preliminary detection campaign, sub branches ${}^RR_{0,2}$, ${}^RR_{0,4}$ and the set of ${}^RQ_{0,2}$ through ${}^RQ_{0,4}$ of the π band were probed. For all scans performed during the preliminary NH2 detection campaign, the parameters remained constant. The flow rate was maintained at 11 SLPM with a reactor pressure of 1.34 PSIA. The plasma discharge was at 10 kHz with a pulse train duration of 400 ms, and had an SEI of 0.4 J/cm^3. The first successful detection of NH2 within the ammonia plasma reformer was of the absorption feature located at sub branch ${}^RR_{0,2}$ of the $\tilde{A}^2A_1(0{,}10{,}0) \leftarrow \tilde{X}^2B_1(0{,}0{,}0)$ transition Shown in figure 15. This doublet absorption feature centered at 568.232-568.236 nm is the strongest within the R branch, making this feature an ideal candidate for the following parametric studies.

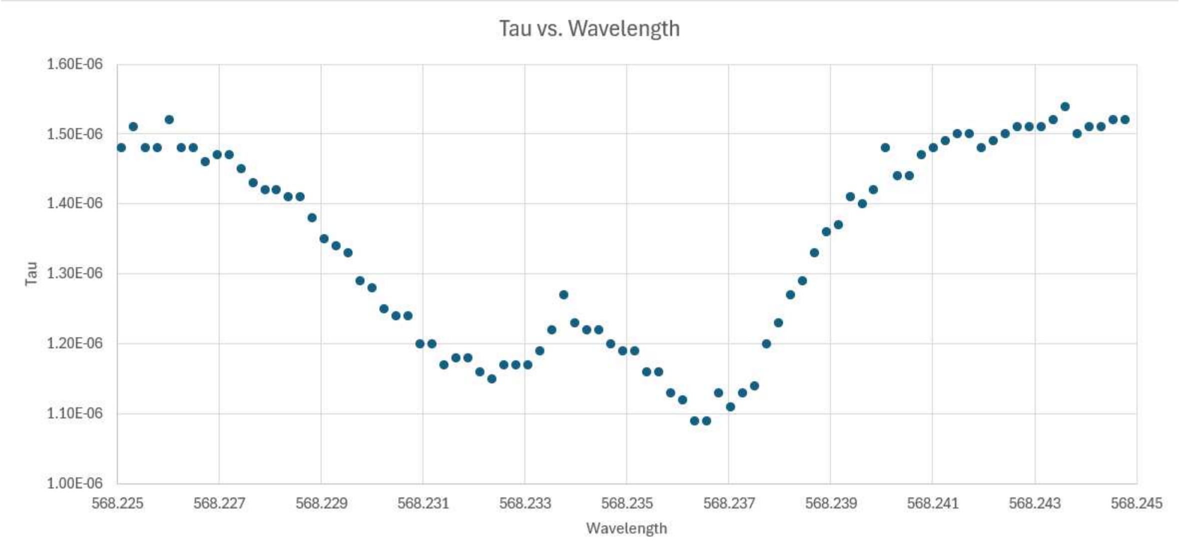

Figure 15: Preliminary Detection of Transition $R_{0,2}$ of NH_2

To confirm that this was in fact an NH_2 detection, other features in the R branch of the pi vibronic sub band were scanned. Branch ${}^{R}R_{0,4}$ was scanned, and the feature was found to be centered at 566.946 nm as shown in figure 16.

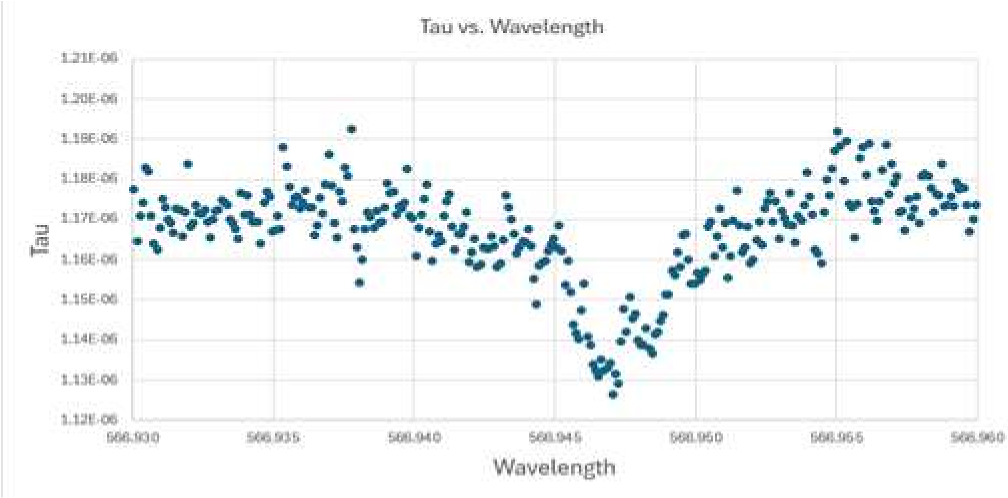

Figure 16: $R_{0,4}$ sub branch detection.

The last scan of the preliminary detection data set was of the Q branch of the pi vibronic sub band. For this scan, the wavelength window was increased to fit multiple features in one scan. In Figure 5, we see the detection of three doublets, ${}^{R}Q_{0,2}$, ${}^{R}Q_{0,3}$, and ${}^{R}Q_{0,4}$. By detecting three features in one scan, coupled with the detection of features within the R branch confirms the detection of the pi vibronic sub band of NH_2 (figure 17).

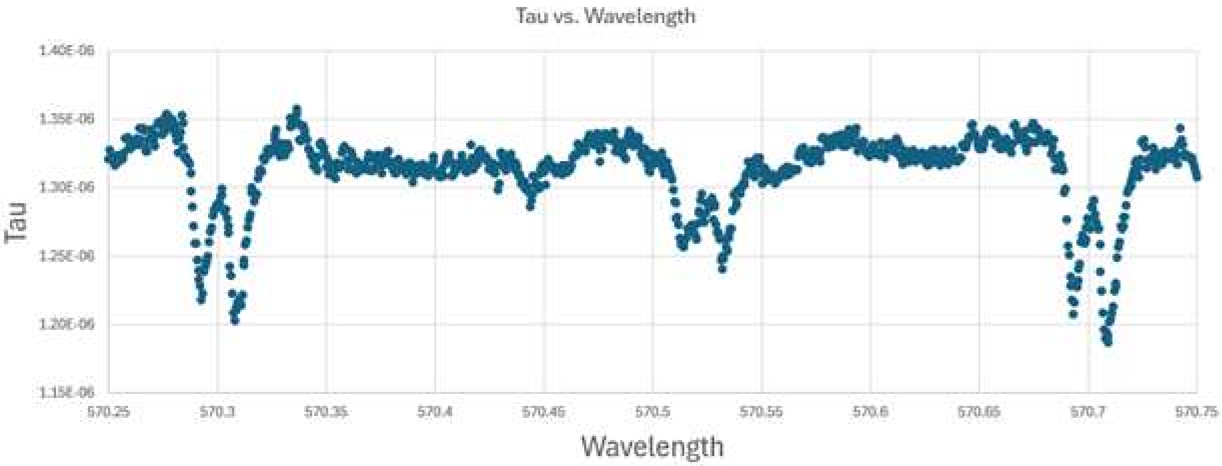

Figure 17: $Q_{0,2}$, $Q_{0,3}$, and $Q_{0,4}$ detection in one scan

This scan including 3 absorption features confirmed the wavelength of the probing beam was calibrated accurately, and that the absorption detected was in fact of NH_2.

4.2.1 Preliminary Results discussion

These preliminary measurements marked a significant milestone for this project, demonstrating the feasibility of CRDS measurements within an optically accessible plasma reformer. While detection of the $\tilde{A}^2A_1(0,10,0) \leftarrow \tilde{X}^2B_1(0,0,0)$ transition have been documented in NH_2 spectroscopy literature such as Dressler et al., the absorption features within this range have rarely been used to measure concentrations of the amino radical [36]. While this is less ideal for comparing data to published literature, it proves the ability of our laser diagnostic system to detect NH_2 within an ammonia plasma reformer. Existing literature does not discuss the required spectroscopic constants to accurately determine NH_2 concentrations for the $\tilde{A}^2A_1(0,10,0)$ $\leftarrow \tilde{X}^2B_1(0,0,0)$ transition. Successful preliminary detections validate the acquisition of the HR mirrors required to detect NH_2 at the $\tilde{A}^2A_1(0,9,0) \leftarrow \tilde{X}^2B_1(0,0,0)$ electronic transition, a strongly favored transition used in a majority of published literature on NH_2 detection using a variety of spectroscopic methods[16], [18], [39]. A paper of particular interest is the work done by P. J. van den Oever et al.. This paper outlines the specific procedure for the calculations used to derive the NH_2 concentrations from the absorption spectra.

4.2.1 π sub-band sweep

The relative absorption of branches $^{R}R_{0,4}$, $^{R}R_{0,3}$, $^{R}R_{0,2}$, $^{R}R_{0,1}$ and $^{R}R_{0,0}$ the π sub-band were all located in a continuous wavelength scan. To confirm that the absorption detected was at the correct wavelength, a scan of the entire band was performed. The dye laser was used to scan across the wavelength (λ) region from 566.9 nm to 570.9 nm at a rate of 0.04 nm per minute. The change in τ versus λ is shown in Fig. 7. A baseline ring-down time of 1.35 μs was obtained from a baseline fit of figure 18.

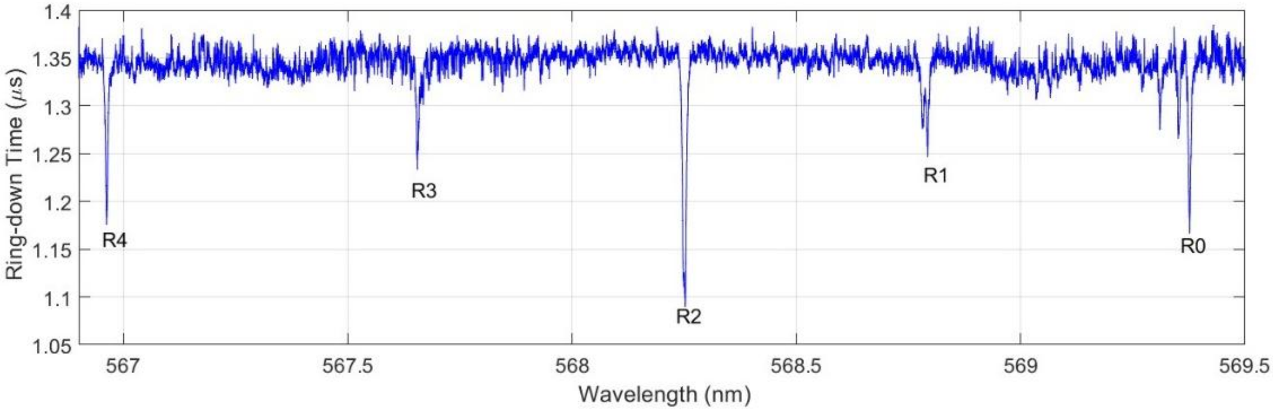

Fig. 18: Ring-down time as a function of laser wavelength.

By overlaying the image of the band from the dressler paper on top of the experimental data scan of figure 7, we can see that not only do the locations of the sub branches line up, but the relative strength of the detected features also correlate with the intensity of the features located on the dressler paper [36](Figure 19).

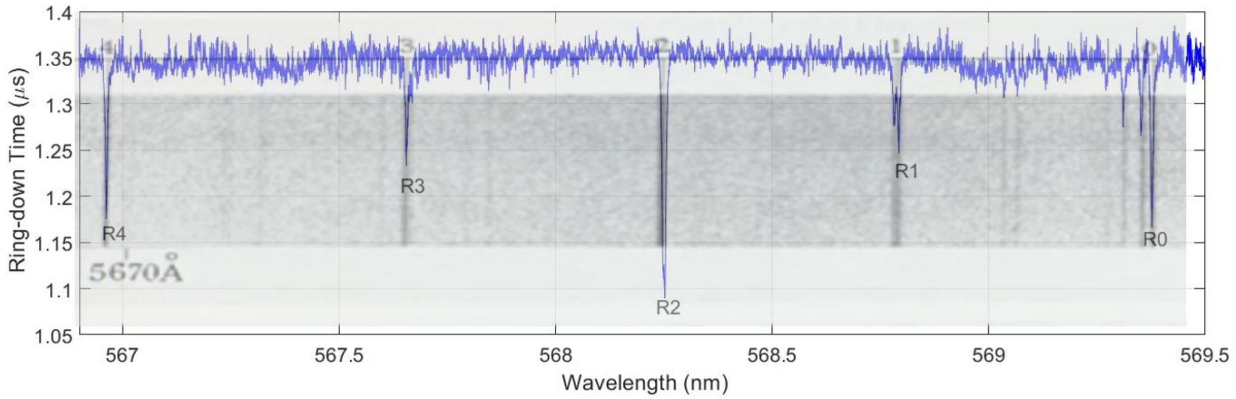

Figure 19: overlay of experimental data over branch from literature

Table 1. Integrated absorption results. Duplicate values for the wavenumbers correspond to the case of doublet.

Transition	Lower rotational state	Upper rotational state	Theoretical wavenumber (cm^{-1})	Abs_Int (cm^{-1})
$^{R}R_{0,4}$	4_{04}	5_{14}	17633.275	5.47e-5
$^{R}R_{0,3}$	3_{03}	4_{13}	17611.742	4.09e-5
$^{R}R_{0,2}$	2_{02}	3_{12}	17593.510 - .370	1.18e-04
$^{R}R_{0,1}$	1_{01}	2_{11}	17576.999 - .673	5.06e-5
$^{R}R_{0,0}$	0_{00}	1_{10}	17559.467 - .728	8.58e-5

The observed transitions from the $\tilde{X}^2B_1(0,0,0)$ to the $\tilde{A}^2A_1(0,10,0)$ respect the c-type selection rules [37], and in particular: $\Delta N = 1$, $\Delta K_a = 1$, and $\Delta K_c = 0$. The lower and upper rotational states are indicated in Table 1, along with the theoretical wavenumber provided in [37]. From the ring-down time signal, we can then determine the absorption of branches $^{R}R_{0,4}$, $^{R}R_{0,3}$, $^{R}R_{0,2}$, $^{R}R_{0,1}$ and $^{R}R_{0,0}$ of the $\tilde{A}^2A_1(0,10,0) \leftarrow \tilde{X}^2B_1(0,0,0)$ band, and determine their relative NH_2 densities by integrating the peaks over wavenumber. Integrated absorption values for these spectral features, corresponding to eqn. (3), are provided in the final column.

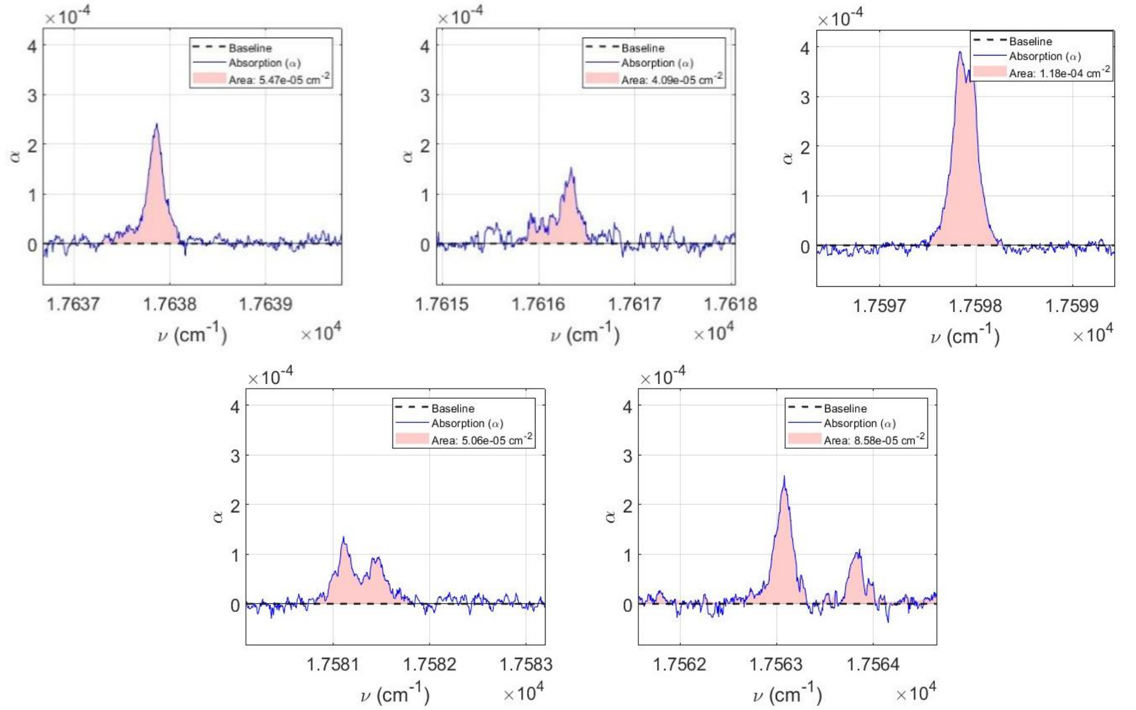

Figure 20: Absorption as a function of wavenumber plots of $^{R}\boldsymbol{R}_{\boldsymbol{0,4}}$, $^{R}\boldsymbol{R}_{\boldsymbol{0,3}}$, $^{R}\boldsymbol{R}_{\boldsymbol{0,2}}$, $^{R}\boldsymbol{R}_{\boldsymbol{0,1}}$, ***and*** $^{R}\boldsymbol{R}_{\boldsymbol{0,0}}$ transitions (from top-left to bottom-right) in the π (0,10,0) vibronic band.

From the spectroscopic scan above (figure 20), the strongest feature $^{R}R_{0,2}$ centered at 17593.510 - .370 cm^{-1} was selected for the parametric and transient studies.

It can be conclusively stated that we are accurately detecting the $\tilde{A}^2A_1(0,10,0) \leftarrow \tilde{X}^2B_1(0,0,0)$ transition. The entire scan of the pi band lining up with the published spectra by dressler et al., provide substantial evidence to the accuracy of our spectroscopic experimental setup. This scan marked the second significant milestone, in which successful scans of the NH_2 absorption spectra of the π vibronic sub-band were able to be processed and data extracted. The integrated absorption of a given feature is a key step towards calculating the total NH_2 density within the reactor. Integrated absorption can be used to quantify relative NH_2 concentrations, as integrated absorption and NH_2 densities share a direct, positive correlation. With this in mind, it is clear that when we refer to table 1, that sub branch $^{R}R_{0,2}$ centered at 17593.510 - .370 cm^{-1} is the strongest feature in the pi vibronic sub band, and a clear choice for the feature of interest for spectroscopic studies while our hardware constraints limit us to this region. A prominent feature such as sub branch ${}^{R}R_{0,2}$ allows for more sensitive measurements at low ammonia decomposition parameters. At low SEI or higher pressures, a stronger feature would give a better idea as to NH_2 densities in these extreme test cases.

4.3 Power Studies

This section details the parametric investigations conducted on both the $\tilde{A}^2A_1(0,10,0) \leftarrow \tilde{X}^2B_1(0,0,0)$ and $\tilde{A}^2A_1(0,9,0) \leftarrow \tilde{X}^2B_1(0,0,0)$ electronic transitions to characterize the effect of energy deposition on NH_2 production. Decomposition of ammonia within a plasma reformer relies on electron impact dissociation, understanding the relationship between input energy and the resulting densities of NH_2 is critical to optimization of reformation efficiency. By systematically varying the supplied voltage (400-900 VDC) and pulse repetition frequency, saturation limits and production efficiency of the NH_2 radical species can be quantified. These parallel studies serve to cross-validate the trends observed in NH_2 production across different spectral regions.

4.3.1 The π sub-band Power Study

For the first parametric study of the ${}^{R}R_{0,2}$ branch of the π vibronic sub-band of the $\tilde{A}^2A_1(0,9,0) \leftarrow \tilde{X}^2B_1(0,0,0)$ transition, PRF and supplied voltage to the pulser were varied to study the effect SEI on the production of NH_2. The number of pulses for the parametric study was maintained at 100 for the entire parametric voltage study, and the feature was measured 6.48 μs after the last pulse. The frequencies studied were every 10 kHz from 10 to 100 kHz where supplied voltages were varied from 450 to 850 VDC with increments of 50 VDC for each PRF increment. This was repeated for both pure ammonia and a mixture of 22% NH_3/78% N_2, both at a flowrate of 45.1 SLPM. This resulted in 144 different scans of tau vs. wavelength of the $R_{0,2}$ branch. From these scans, we can then plot integrated absorption vs. supplied voltage (figure 21).

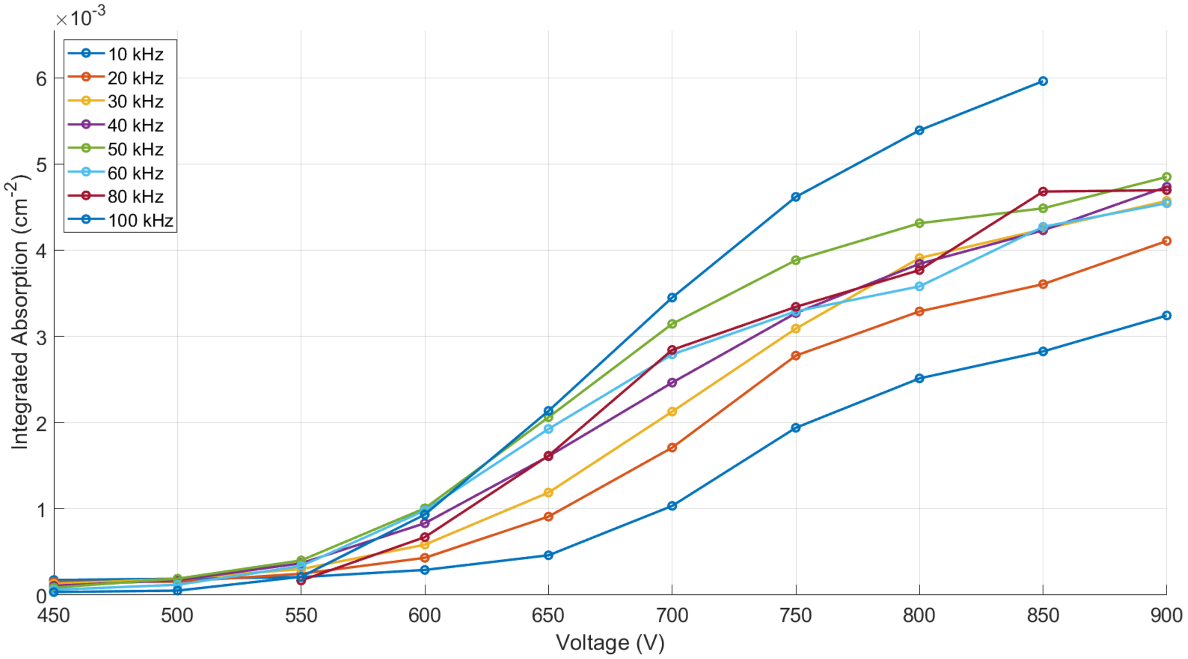

Figure 21: Relative density of NH2 vs. supplied voltage

4.3.2 ε sub-band Power Study

For the $^{P}Q_{1,7}$ branch of the ε band of the $\tilde{A}^2A_1(0,9,0) \leftarrow \tilde{X}^2B_1(0,0,0)$ transition power study, a reactor pressure of 1.34 PSIA and a pure ammonia flow rate of 12 SLPM was maintained for the duration of this study. A pulse train of 400 pulses at a pulse repetition frequency of 10 kHz was held constant. The feature was measured 0.08 ms after the last pulse and measured at supplied voltages 400-950 VDC, or a range of 0.02 to 1.09 SEI. A plot of Integrated absorption vs. wavenumber for each SEI case, and relative NH_2 concentrations vs. SEI are then created using the data collected from parametric study (figure 22).

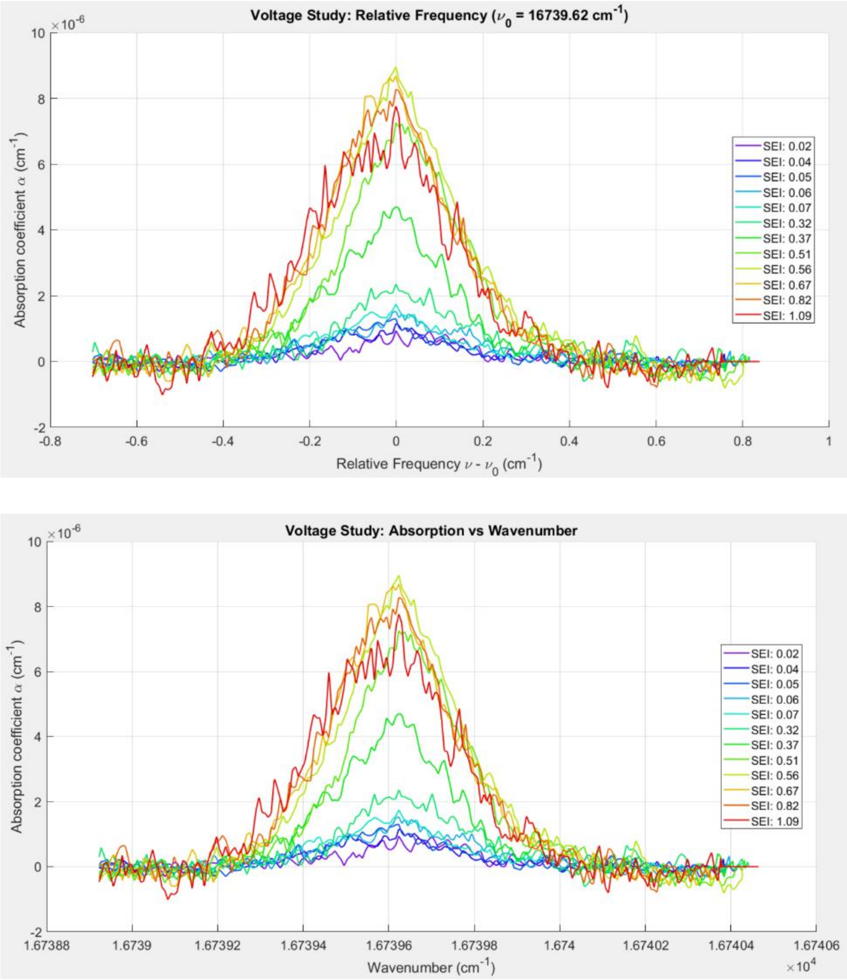

Figure 22: figure A; true frequency scale of feature. figure b; Relative frequency scaling of feature

A clear trend is observed where increasing SEI results in an increase in absorption. The production limit of NH_2 seems to form around 0.56 SEI, where the amount of absorption with increased SEI stays relatively constant. These results align with expected behavior, as the energy input into the plasma affects the amount of decomposition that occurs. In figure 21, it can be seen that there is not an even distribution of absorption across the SEI. To better visualize this behavior, figure 22 plots NH_2 density vs. SEI.

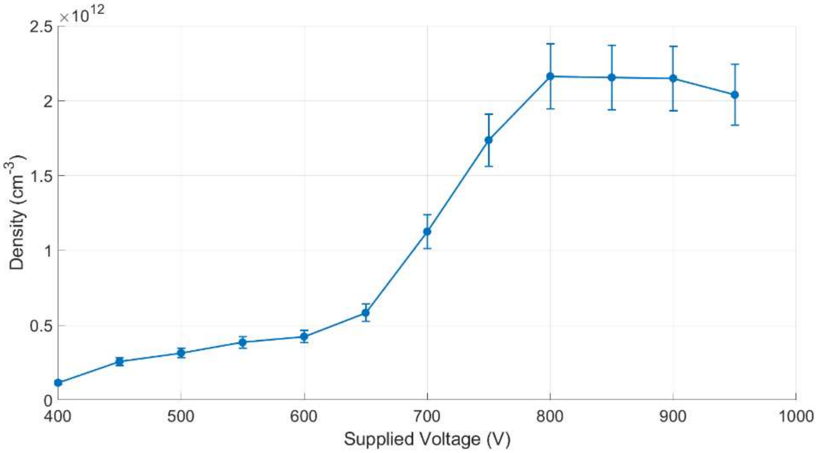

Figure 23: NH_2 density vs. Supplied voltage and density vs. SEI

Figure 23 shows a clear increase in NH_2 concentration with supplied voltage. Note the low concentrations of NH_2 at voltages below 600 VDC. Papers show that a minimum SEI is required to create homogeneous plasma discharges and not coronas. Once supply voltage increases above 600 VDC in our data, we see a sharp increase in NH_2 production. By 800 VDC, NH_2 concentrations level out and a saturation effect is observed. The slow decrease in density after 800 VDC can be attributed to propagated error.

4.3.1 Power Study Discussion

Due to lack of literature regarding the $\tilde{A}^2A_1(0,10,0) \leftarrow \tilde{X}^2B_1(0,0,0)$ transition, determining the densities of NH_2 for the absorption feature located at 17593.510 - .370 cm^{-1} were not possible. However, relative density of NH_2 can be represented as integrated absorption, as the relationship between actual NH_2 density and integrated absorption is both positive and linear. Generalized assumptions of spectroscopic constants rotational and vibrational temperatures related to the $\tilde{A}^2A_1(0,9,0) \leftarrow \tilde{X}^2B_1(0,0,0)$ transition were made to calculate the densities of NH_2 based off of existing literature on this specific transition. In both figure 21 and 23, an SEI threshold limits the NH_2 production at low SEI values where plasma energy is low, and the two distinct plasma regimes are observed. For supplied voltages less than 600 VDC, the reactor is operating in the corona discharge regime. In both power studies, the data is purposefully presented in power supply voltage. It can be seen in the plasma characterization results that our ability to measure SEI accurately with our probes was not possible and did not properly characterize the relationship between plasma energy and NH_2 concentrations. While supplied voltage does not allow for direct comparison of our plasma source, it provides a clear trend of NH_2 production with increased energy. The use of relative density and energy measurements in the presented data provides observable trends consistent across absorption transitions. In Figure 17,

4.4 Transient Studies

Transient studies performed on both the π and ε vibronic sub bands enable characterization of temporal evolution and stability of the NH_2 fuel radical in the post discharge environment. In a pulsed nanosecond plasma reactor, a cycle of discharges consists largely of no discharge formation, and thus the kinetics and chemistry that occur in the inter-pulse time is the dominant transient regime for quantifying NH_2 concentrations. Understanding the decay rate of NH_2 concentrations is critical to maximizing combustion efficiency of the reformed mixtures. Transient results of NH_2 will enhance plasma reactor parameters to optimize ammonia dissociation.

4.4.1 π sub-band Transient Study

The ${}^{R}R_{0,2}$ branch of the π vibronic sub-band of the $\tilde{A}^2A_1(0,9,0) \leftarrow \tilde{X}^2B_1(0,0,0)$ transition was scanned after the formation of plasma to determine the decay rate of NH_2 concentrations within the reactor. The transient study of the used a constant SEI and number of pulses in a mixture of 22% NH_3/78% N_2. A decay of NH_2 was observed over a millisecond scale. The PRF was 10 kHz, with a pulse train 400 pulses long. Measurements were taken in increments of 10 ms from 0 to 60 ms from the last pulse. The Ammonia flowrate was 45.1 SLPM, at a pressure of 77 Torr. Tau vs. wavelength was found for each delay to determine change in relative concentrations. The integrated absorption vs. pulse delay can then be plotted in figure 24 below.

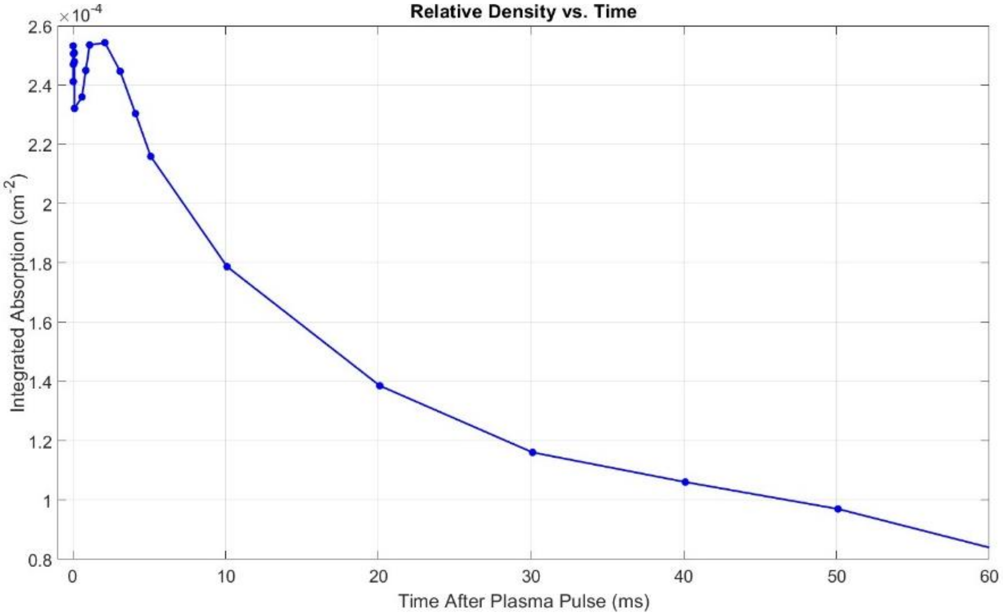

Figure 24: Relative concentration of NH_2 vs. Delay

4.4.2 ε sub-band Transient Study

For the $^{P}Q_{1,7}$ branch of the ε band of the $\tilde{A}^2A_1(0,9,0) \leftarrow \tilde{X}^2B_1(0,0,0)$ transition, SEI of 0.56 was maintained, nd the branch was scanned from 0 to 30.08 ms after the last pulse. Plasma parameters were held constant at a pulse repetition frequency of 10 kHz for a 400 pulse burst. A reactor pressure of 1.34 PSIA and a pure ammonia flow rate of 12 SLPM was maintained for the duration of this study. This data is then plotted in figures of integrated absorption vs. wavenumber.

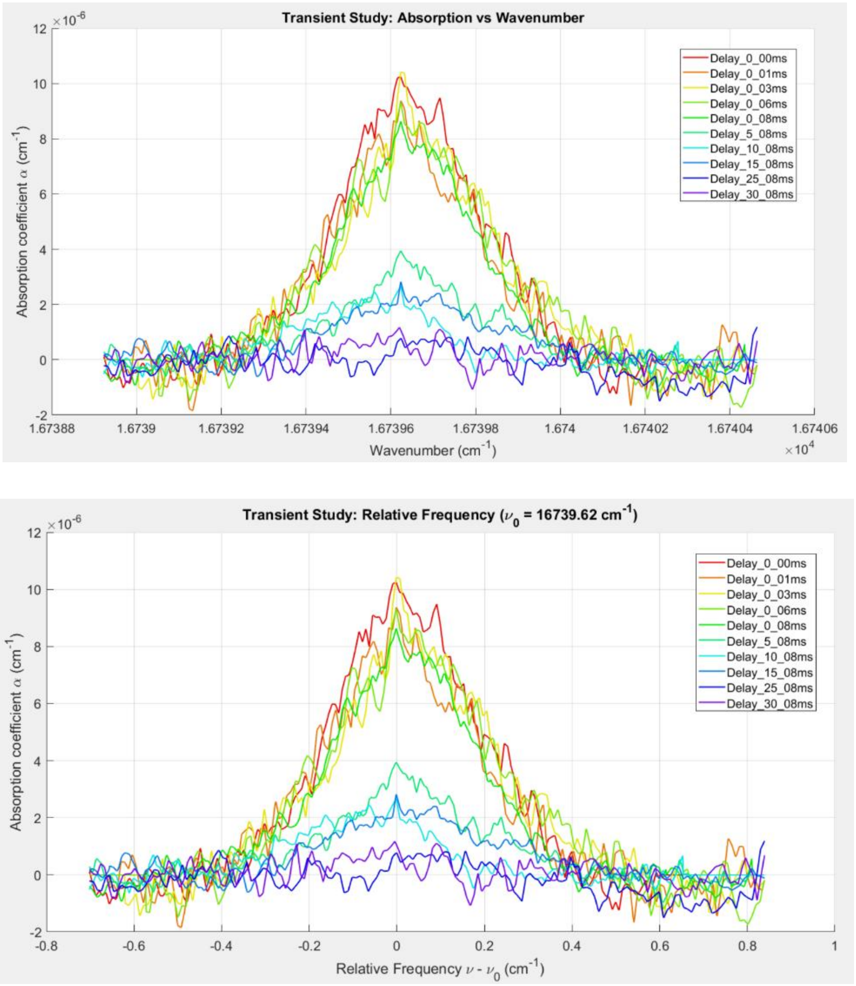

Figure 25: figure A; true frequency scale of feature. figure b; Relative frequency scaling of feature

In figure 25, a non-linear trend between delay and absorption can be seen. Relative NH_2 densities fall rapidly. Plotting data from figure 25 as NH_2 densities vs. delay is shown in figure 26 below.

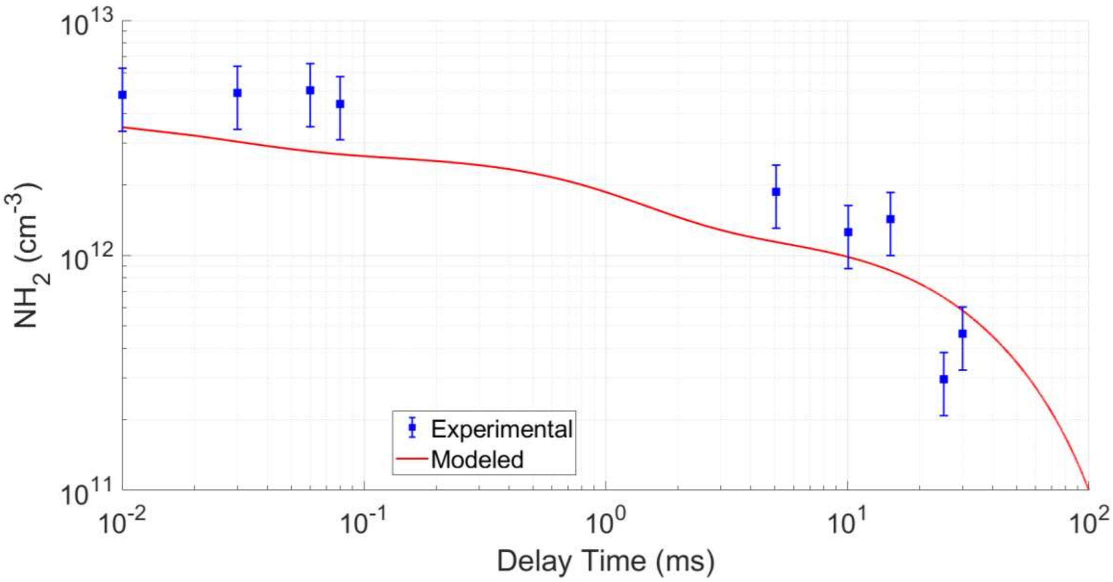

Figure 26: NH_2 concentrations vs. Delay

In figure 26, it can be seen that measurement delay has a significant effect on the concentrations of NH_2.

4.4.3 Transient Study Discussion

For both $\tilde{A}^2A_1(0,10,0) \leftarrow \tilde{X}^2B_1(0,0,0)$ and $\tilde{A}^2A_1(0,9,0) \leftarrow \tilde{X}^2B_1(0,0,0)$ electronic transitions, an exponential decay of NH_2 densities are observed at different time scales. For the ε transient study, NH_2 concentrations quickly decrease after the plasma formation at 0 ms. Using a log-log plot, two distinct decay modes are observed. At earlier time-steps below 0.1 ms, high energy species with longer lifetimes continue to ionize, contributing to NH_2 production. In later time steps above 5 ms, we see a quick decay in NH_2 concentrations as molecules begin to recombine into less reactive species. The decay observed at the pi sub-band was significantly longer than the one observed at the e transition. Attempts were made to measure NH_2 densities at the e sub band after 30 ms were lost in the noise and thus inconclusive. Contrary to the decay of

NH_2 at the pi sub band, where clear absorption of NH_2 was measured in the entire inter-burst time between pulse trains. In both studies, NH_2 absorption measurements within 45 us of the last pulse were affected by the jitter of the q-switch that propagated to plasma formation because the q-switch is the clock of the system.

Future Work

CHAPTER 5

CONCLUSION AND FUTURE WORK

5.1 Summary of Key Accomplishments and Conclusion

The primary objective of this research was to design, construct, and validate a nanosecond pulsed plasma reactor capable of reforming ammonia, and to integrate a Cavity Ring-Down Spectroscopy (CRDS) diagnostic for the quantitative detection of the amidogen radical NH_2. The results presented within this thesis demonstrate successful operation of the ammonia plasma reactor and confirm the viability of CRDS as a non-intrusive, in-situ probe for intermediate radicals within a dielectric barrier discharge.

A major portion of this work focused on system design and integration. Careful consideration was given to material and component selection. Specifically, ammonia gas delivery necessitated the use of corrosion-resistant materials and adherence to the desired flow conditions.

Significant effort was dedicated to the stabilization of the plasma discharge and reduction of electro-magnetic interference (EMI). Through iterative testing of the high voltage pulser, a stable operating regime was identified that allowed for a consistent discharge frequency. It was found that by lowering the total number of pulses within a pulse train, supply voltages from 400-950 and pulse repetition frequencies from 10-100 kHz were achieved.

A primary hurdle encountered was the electromagnetic noise induced by the plasma discharge within the reactor. In the Initial reactor design, the Faraday cage mounted directly to the optical table where the table surface served as the bottom of the Faraday cage. This configuration caused the table to act as an antenna for the electromagnetic noise. When the Faraday cage was mounted directly on the table along with the reactor, significant EMI was detected by the PMT. This PMT is very sensitive to weak electromagnetic signals and was saturated by the strong EMI of the plasma discharge. Making it impossible to acquire a clean CRDS signal. It was later established that the Faraday cage should be electrically isolated from the optical table such that the ground of the reactor is connected only to the Faraday cage with no gaps to arc directly to the optical table. Placing the Faraday cage on top of insulating materials such as wood and plastic sheeting lifting the cage off the optical table, EMI was effectively mitigated.

The CRDS system achieved a baseline tau of 2.1 us due to an optimized alignment procedure, achieving 96% of the theoretical baseline tau of the HR cavity. Multiple rotational features were identified across multiple absorption bands that matched the locations of transition lines in literature. Parametric studies of power within the plasma reactor using cavity ring down spectroscopy revealed or confirmed the presence of two distinct plasma regimes operating regimes within the plasma reactor. This establishes that the reactor must maintain a supplied voltage of above 600 VDC (or an equivalent Specific energy input), such that the plasma discharge is homogenous and fills the entire volume of the reactor. The time-resolved measurements of energy within the plasma discharge persisted up to 60 milliseconds for the π band transition and up to 40 milliseconds in the ε transition but most likely persisted up to the 60 milliseconds of time as well but was unmeasurable due to the noise drowning out the potential spectrum absorption signal. This showed that the NH_2 was present within the reactor for much longer than the inter-pulse time of 0.1 ms, resulting in a much longer transient lifetime that was initially assumed in modeling.

In summary, this work has established a robust experimental testbed. The successful measurement of absolute NH_2 densities provides the critical first step towards validating kinetic models for plasma reformation, offering a pathway to optimized hydrogen generation technologies.

5.3 Recommendations for Future Research

While significant progress has been made to quantify NH_2 concentrations within an ammonia plasma reformer, the experiment would benefit greatly from additional CRDS measurements, Optical Emission Spectroscopy (OES), and thermal imaging.

The current reactor design, while functional, presents challenges regarding optical stability and maintenance. The location of the fine adjustment screws for the HR cavity proved difficult to access within the Faraday cage. While adjustment was easy due to the fine pitch of the adjustment screws, their drift from alignment made keeping cavity ring down baseline Tau values consistent difficult. In addition, the plasma discharge dissociating the ammonia within the reactor resulted in a buildup of deposits on the HR mirrors, contributing to the decrease in baseline Tau over time. A mirror purging system, where a flow of inert gas can be blown over the mirrors to help prevent the buildup of such deposits could increase the stability of the baseline Tau over time. Positioning of the HR cavity here the gas outlet for a future reactor design could maximize NH_2 detection. While the outer copper electrode was meshed to allow for visual optical access to the reactor chamber, the use of a full outer electrode on the effect of ammonia decomposition should be explored.

With the diagnostic method validated, future campaigns can focus on our broader range of operating conditions. Exploring the two different plasma discharge regimes seen within the reactor at varied energy could be greater explored to understand the optimal efficiency for the use of this reactor for hydrogen generation.

Acknowledgements

Thank you to NSF for funding of the project (grant number: 2236512), the lending of the high voltage pulser from the Air Force Research Laboratory, collaboration efforts from Technion university, and Colorado state for hosting the research.

References

[1] Yoshitsuga Kojima, "A Green Ammonia Economy," in *Oxford Art Online*, Oxford University Press, 2020. doi: 10.1093/oao/9781884446054.013.90000369090.

[2] M. Aziz, A. T. Wijayanta, and A. B. D. Nandiyanto, "Ammonia as Effective Hydrogen Storage: A Review on Production, Storage and Utilization," *Energies*, vol. 13, no. 12, p. 3062, Jun. 2020, doi: 10.3390/en13123062.

[3] "2023-Toyota-Mirai_Product-Info-Guide."

[4] B. Heid, C. Martens, and A. Orthofer, "How hydrogen combustion engines can contribute to zero emissions".

[5] Volvo, "Hydrogen fuel cells and combustion engines." Volvo, volvo.com. [Online]. Available: https://www.volvogroup.com/en/sustainable-transportation/sustainable-solutions/hydrogen-fuel-cells.html

[6] J. Hwang, K. Maharjan, and H. Cho, "A review of hydrogen utilization in power generation and transportation sectors: Achievements and future challenges," *International Journal of Hydrogen Energy*, vol. 48, no. 74, pp. 28629–28648, Aug. 2023, doi: 10.1016/j.ijhydene.2023.04.024.

[7] A. Valera-Medina, H. Xiao, M. Owen-Jones, W. I. F. David, and P. J. Bowen, "Ammonia for power," *Progress in Energy and Combustion Science*, vol. 69, pp. 63–102, Nov. 2018, doi: 10.1016/j.pecs.2018.07.001.

[8] J. Sun, N. Zhao, and H. Zheng, "A comprehensive review of ammonia combustion: Fundamental characteristics, chemical kinetics, and applications in energy systems," *Fuel*, vol. 394, p. 135135, Aug. 2025, doi: 10.1016/j.fuel.2025.135135.

[9] O. Mathieu and E. L. Petersen, "Experimental and modeling study on the high-temperature oxidation of Ammonia and related NOx chemistry," *Combustion and Flame*, vol. 162, no. 3, pp. 554–570, Mar. 2015, doi: 10.1016/j.combustflame.2014.08.022.

[10] D. Pugh *et al.*, "An investigation of ammonia primary flame combustor concepts for emissions reduction with OH*, NH2* and NH* chemiluminescence at elevated conditions," *Proceedings of the Combustion Institute*, vol. 38, no. 4, pp. 6451–6459, 2021, doi: https://doi.org/10.1016/j.proci.2020.06.310.

[11] J. Choe, W. Sun, T. Ombrello, and C. Carter, "Plasma assisted ammonia combustion: Simultaneous NOx reduction and flame enhancement," *Combustion and Flame*, vol. 228, pp. 430–432, Jun. 2021, doi: 10.1016/j.combustflame.2021.02.016.

[12] P. J. Van Den Oever *et al.*, "Density and production of NH and NH2 in an Ar–NH3 expanding plasma jet," *Journal of Applied Physics*, vol. 98, no. 9, p. 093301, Nov. 2005, doi: 10.1063/1.2123371.

[13] I. Hadj Bachir, T. R. Huet, J.-L. Destombes, and M. Vervloet, “A Combined Analysis of Laser Optogalvanic and Fourier Transform Emission Spectra of NH2near its Barrier to Linearity,” *Journal of Molecular Spectroscopy*, vol. 193, no. 2, pp. 326–353, Feb. 1999, doi: 10.1006/jmsp.1998.7752.

[14] J. B. Halpern, G. Hancock, M. Lenzi, and K. H. Welge, “Laser induced fluorescence from NH2(2 *A* 1). State selected radiative lifetimes and collisional de-excitation rates,” *The Journal of Chemical Physics*, vol. 63, no. 11, pp. 4808–4816, Dec. 1975, doi: 10.1063/1.431223.

[15] S. T. Gibson, J. P. Greene, and J. Berkowitz, “Photoionization of the amidogen radical,” *The Journal of Chemical Physics*, vol. 83, no. 9, pp. 4319–4328, Nov. 1985, doi: 10.1063/1.449045.

[16] H. Tang, D. Ezendeeva, and G. Magnotti, “Simultaneous measurements of NH2 and major species and temperature with a novel excitation scheme in ammonia combustion at atmospheric pressure,” *Combustion and Flame*, vol. 250, p. 112639, Apr. 2023, doi: 10.1016/j.combustflame.2023.112639.

[17] M. Kroll, “The fluorescence spectrum of NH2 excited by a cw dye laser,” *The Journal of Chemical Physics*, vol. 63, no. 1, pp. 319–325, Jul. 1975, doi: 10.1063/1.431101.

[18] R. M. Green and J. A. Miller, “The measurement of relative concentration profiles of NH2 using laser absorption spectroscopy,” *Journal of Quantitative Spectroscopy and Radiative Transfer*, vol. 26, no. 4, pp. 313–327, Oct. 1981, doi: 10.1016/0022-4073(81)90126-6.

[19] J. K. Lefkowitz, “Plasma Reforming of Ammonia for Improved Combustion Performance”.

[20] P. N. Johnson, T. S. Taneja, and S. Yang, “Plasma-based global pathway analysis to understand the chemical kinetics of plasma-assisted combustion and fuel reforming,” *Combustion and Flame*, vol. 255, p. 112927, Sep. 2023, doi: 10.1016/j.combustflame.2023.112927.

[21] J. A. Andersen, K. Van ’T Veer, J. M. Christensen, M. Østberg, A. Bogaerts, and A. D. Jensen, “Ammonia decomposition in a dielectric barrier discharge plasma: Insights from experiments and kinetic modeling,” *Chemical Engineering Science*, vol. 271, p. 118550, May 2023, doi: 10.1016/j.ces.2023.118550.

[22] G. Faingold, O. Kalitzky, and J. K. Lefkowitz, “Plasma reforming for enhanced ammonia-air ignition: A numerical study,” *Fuel Communications*, vol. 12, p. 100070, Sep. 2022, doi: 10.1016/j.jfueco.2022.100070.

[23] G. Faingold and J. K. Lefkowitz, “A numerical investigation of NH3/O2/He ignition limits in a non-thermal plasma,” *Proceedings of the Combustion Institute*, vol. 38, no. 4, pp. 6661–6669, 2021, doi: 10.1016/j.proci.2020.08.033.

[24] I. B. Matveev, S. I. Serbin, and A. E. Zinchenko, “A High-Concentration NO_x Production System—Part 1: Optimization of the Quenching Rate,” *IEEE Trans. Plasma Sci.*, vol. 50, no. 6, pp. 1630–1634, Jun. 2022, doi: 10.1109/TPS.2021.3134689.

[25] S. Mashruk *et al.*, “Numerical Analysis on the Evolution of NH_2 in Ammonia/hydrogen Swirling Flames and Detailed Sensitivity Analysis under Elevated Conditions,” *Combustion Science and Technology*, vol. 195, no. 6, pp. 1251–1278, Apr. 2023, doi: 10.1080/00102202.2021.1990897.

[26] U. Kogelschatz, “Dielectric-Barrier Discharges: Their History, Discharge Physics, and Industrial Applications,” *Plasma Chemistry and Plasma Processing,* vol. 23, no. 1, Mar. 2003, doi: 0272-4324 03 0300-0001 0.

[27] R. Brandenburg, “Dielectric barrier discharges: progress on plasma sources and on the

understanding of regimes and single filaments," *Plasma Sources Sci. Technol.*, vol. 26, no. 5, p. 053001, Mar. 2017, doi: 10.1088/1361-6595/aa6426.

[28] S. K. Kundu, E. M. Kennedy, V. V. Gaikwad, T. S. Molloy, and B. Z. Dlugogorski, "Experimental investigation of alumina and quartz as dielectrics for a cylindrical double dielectric barrier discharge reactor in argon diluted methane plasma," *Chemical Engineering Journal*, vol. 180, pp. 178–189, Jan. 2012, doi: 10.1016/j.cej.2011.11.039.

[29] J. E. MOYALt, "THEORY OF THE IONIZATION CASCADE".

[30] J. Li, C. Ma, S. Zhu, F. Yu, B. Dai, and D. Yang, "A Review of Recent Advances of Dielectric Barrier Discharge Plasma in Catalysis," *Nanomaterials*, vol. 9, no. 10, p. 1428, Oct. 2019, doi: 10.3390/nano9101428.

[31] S. Sinha, C. Jeyaseelan, G. Singh, T. Munjal, and D. Paul, "Spectroscopy—Principle, types, and applications," in *Basic Biotechniques for Bioprocess and Bioentrepreneurship*, Elsevier, 2023, pp. 145–164. doi: 10.1016/B978-0-12-816109-8.00008-8.

[32] "Interstellar spectra." Cosmos at Your Doorstep, website, Jul. 17, 2018. [Online]. Available: https://cosmosatyourdoorstep.com/2018/07/17/interstellar-spectra/

[33] G. Berden and R. Engeln, Eds., *Cavity ring-down spectroscopy: techniques and applications*. Chichester, U.K: Wiley, 2009.

[34] Kenneth W. Busch and Marianna A. Busch, *Cavity-Ringdown Spectroscopy: An Ultratrace-Absorption Measurement Technique*. 1999.

[35] A. P. Yalin and R. N. Zare, "Effect of Laser Lineshape on the Quantitative Analysis of Cavity Ring-Down Signals," vol. 12, no. 8, 2002.

[36] K. Dressler and D. A. Ramsay, "The electronic absorption spectra of NH2 and ND2".

[37] S. C. Ross, F. W. Birss, M. Vervloet, and D. A. Ramsay, "The absorption spectrum of NH2 in the region 5300 to 6800 Å," *Journal of Molecular Spectroscopy*, vol. 129, no. 2, pp. 436–470, Jun. 1988, doi: 10.1016/0022-2852(88)90048-3.

[38] D. L. Rusterholtz, D. A. Lacoste, G. D. Stancu, D. Z. Pai, and C. O. Laux, "Ultrafast heating and oxygen dissociation in atmospheric pressure air by nanosecond repetitively pulsed discharges," *J. Phys. D: Appl. Phys.*, vol. 46, no. 46, p. 464010, Nov. 2013, doi: 10.1088/0022-3727/46/46/464010.

[39] P. J. Van Den Oever *et al.*, "N, NH, and NH2 radical densities in a remote Ar–NH3–SiH4 plasma and their role in silicon nitride deposition," *Journal of Applied Physics*, vol. 100, no. 9, p. 093303, Nov. 2006, doi: 10.1063/1.2358330.